J. Fluid Mech. (2014), *vol.* 754, *pp.* 122–160.
doi:10.1017/jfm.2014.393

Highly resolved pulsatile flows through prosthetic heart valves using the entropic lattice-Boltzmann method

B. Min Yun[1], L. P. Dasi[2], C. K. Aidun[1,3] and A. P. Yoganathan[1,4,†]

[1]G. W. Woodruff School of Mechanical Engineering, Georgia Institute of Technology, 801 Ferst Drive, Atlanta, GA 30332, USA

[2]Department of Mechanical Engineering, Colorado State University, Campus Delivery 1374, Fort Collins, CO 80523, USA

[3]Parker H. Petit Institute for Bioengineering and Bioscience, Georgia Institute of Technology, 315 Ferst Drive, Atlanta, GA 30332, USA

[4]Wallace H. Coulter Department of Biomedical Engineering, Georgia Institute of Technology and Emory University, 313 Ferst Drive, Atlanta, GA 30332, USA

(Received 4 September 2013; revised 24 April 2014; accepted 3 July 2014; first published online 30 July 2014)

Prosthetic heart valves have been widely used to replace diseased or defective native heart valves. Flow through bileaflet mechanical heart valves (BMHVs) have previously demonstrated complex phenomena in the vicinity of the valve owing to the presence of two rigid leaflets. This study aims to accurately capture the complex flow dynamics for pulsatile flow through a 23 mm St Jude Medical (SJM) Regent™ BMHV. The lattice-Boltzmann method (LBM) is used to simulate pulsatile flow through the valve with the inclusion of reverse leakage flow at very high spatiotemporal resolution that can capture fine details in the pulsatile BMHV flow field. For higher-Reynolds-number flows, this high spatiotemporal resolution captures features that have not been observed in previous coarse resolution studies. In addition, the simulations are able to capture with detail the features of leaflet closing and the asymmetric b-datum leakage jet during mid-diastole. Novel flow physics are visualized and discussed along with quantification of turbulent features of this flow, which is made possible by this parallelized numerical method.

Key words: biomedical flows, turbulence simulation, vortex dynamics

1. Introduction

Native heart valves, which work to maintain unidirectional blood flow in the heart, may become defective owing to birth defects or disease. Prosthetic valves have been used as replacements for defective valves for over 50 years, and mechanical heart valves are the most popular option (Black & Drury 1994). Bileaflet mechanical heart valves (BMHVs) are the most popular design owing to superior durability, function and bulk flow haemodynamics, and account for 80 % (Yoganathan *et al.* 2003) of implanted mechanical valves.

† Email address for correspondence: ajit.yoganathan@bme.gatech.edu

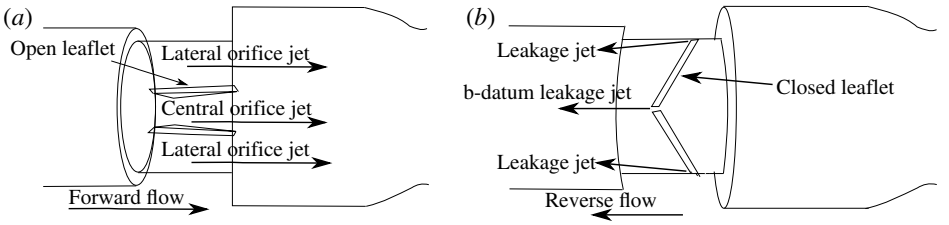

FIGURE 1. Schematic of (*a*) forward and (*b*) reverse BMHV flows and the popular SJM valve design.

Figure 1 demonstrates a BMHV in the forward and reverse flow phases. The circular wall of the valve is referred to as the valve housing. During forward flow, most of the blood flows through three orifices formed by the open leaflets (figure 1*a*). The three jets during forward flow are the two lateral orifices and the central orifice. During reverse flow (figure 1*b*), there is leakage flow through the hinges, the gap between the closed leaflets and valve housing (not shown) and the central b-datum plane.

Despite long-term design evolution, BMHVs still cause serious complications such as platelet activation and thromboembolism (Giersiepen *et al.* 1990; Dumont *et al.* 2007). These complications are owing to non-physiologic shear stress levels imposed on blood elements by complex flows through BMHVs (Ellis *et al.* 1996). This may lead to thrombus formation in the valves, and emboli may detach and become lodged in smaller blood vessels, leading to stroke and death. Experimental studies examining these complex flows are generally limited by the lack of optical access within the valve, particularly close to the leaflets. This prevents full view of complex pulsatile BMHV flows, particularly during leaflet closing and diastole. An initial study showed blood damage effects of reverse flow are as significant as forward flow (Lamson *et al.* 1993). Several studies have shown the potential for b-datum reverse jets to induce platelet activation (Fallon *et al.* 2006; Krishnan *et al.* 2006), and passive flow control measures have been attempted to reduce thromboembolic potential in these reverse flows (Dasi *et al.* 2008; Murphy *et al.* 2010).

An advantage of computational fluid dynamics (CFD) to explore BMHV flows is the ability to model 3D flows with high spatiotemporal resolution, whereas experimental studies are mostly limited to data in 2D planes. CFD methods are also able to capture intricate flow dynamics within or very close to the valve region. The vorticity dynamics in pulsatile BMHV flows were explored in one dual experimental–computational study (Dasi *et al.* 2007). 3D vorticity dynamics were explored computationally, showing rich, complex 3D vortex structures with greater clarity than experimental results. Computational simulations of flow through BMHVs have also included dynamic leaflet motion using two-way fluid–structure interaction (FSI), including one study by De Tullio *et al.* (2010) that employed an immersed boundary method to simulate pulsatile 3D flow through a BMHV. Computational methods have also expanded in modelling beyond simplified *in vitro* geometries, focusing on more physiological geometries that include bends in the domain and more anatomical features. Studies by Borazjani, Ge & Sotiropoulos (2008), Borazjani & Sotiropoulos (2010) examined pulsatile 3D flow through a BMHV in an anatomic aorta, characterizing the effect of realistic geometries on the BMHV flow fields.

Turbulence is of high interest for BMHV flows, as turbulent flows and Reynolds stresses are often correlated to high levels of blood damage (Sallam & Hwang 1984; Kameneva *et al.* 2004). The dissipation of kinetic energy in turbulent flows is also

important for prosthetic valve flows, as this can be related to irreversible pressure loss, a potentially serious complication for cardiovascular flows (Dyverfeldt *et al.* 2013). The smallest Kolmogorov scales for BMHV flows have been estimated of the order of tens of micrometres, which is several times larger than the size of suspended blood elements such as red blood cells and platelets. However, it has been proposed by Antiga & Steinman (2009) that turbulent velocity fluctuations could relate to increased viscous shear stresses, owing to energy dissipation that is caused by cell–cell interaction. Thus, turbulence that is caused by BMHVs may be related to the increased potential for blood damage.

Although features such as Reynolds stresses have been calculated in BMHV flows (Grigioni *et al.* 2005; Ge *et al.* 2008; De Tullio *et al.* 2010), turbulence has not been well examined. Liu, Lu & Chu (2000) calculated energy spectra against temporal frequency for BMHV flows using laser Doppler velocimetry measurements, demonstrating a $-5/3$rd slope and the presence of an inertial range. However, this quantification of turbulence in BMHV flows has not been performed using computational studies, nor has energy spectra been plotted against wavenumber in order to relate spatial scales of BMHV flows to inertial or dissipative ranges of the energy cascade. Understanding turbulence in BMHV flows may help to clarify how the presence of these prostheses is related to the severe complications associated with these devices.

The objective of this study is to employ a high-performance lattice-Boltzmann method (LBM) to model pulsatile BMHV flow with high spatiotemporal resolution, and explore novel aspects of the flow physics. This includes modelling of the leaflet closing and mid-diastolic flow phases, where flow features within or near the valve can be delineated. Leakage jet velocities and fluid shear stresses during these flow regimes are also quantified, which can be associated with blood damage that occurs in diastolic flows. Turbulent features are also quantified in BMHV flow through the calculation of turbulent energy dissipation rates and plotting of energy spectra against wavenumber for BMHV peak flow. This LBM is able to capture fine-scale features of the flow throughout the cardiac cycle with spatial resolution close to the Kolmogorov scales owing to its high parallel performance. The numerical method is described in detail with validation against experiments in Part 1 of this work (Yun *et al.* 2014*a*).

The paper is organized as follows. In § 2, we briefly overview the LBM and the numerical set-up. In § 3, we simulate pulsatile BMHV flow and detail 2D and 3D numerical visualizations at various timepoints of the cardiac cycle, followed by a focus on the leaflet closing phase, mid-diastolic reverse flow phase and quantification of turbulent features. In § 4, we discuss the results of our simulations and their implications. Concluding remarks are made in § 5.

2. Methodology

2.1. *LBM*

The LBM is a numerical method used for solving fluid flow, and is based on kinetic gas theory. Its use in modelling flows has been well documented (Ladd 1994; Aidun & Lu 1995; Aidun, Lu & Ding 1998; Ladd & Verberg 2001; Ding & Aidun 2003). The method described by Aidun *et al.* and that employed in this study is a D3Q19, single-relaxation method. The solution of the lattice-Boltzmann equations converges to solve the Navier–Stokes equations for fluid flow, and FSIs are dealt with via the ‘standard bounce-back’ (SBB) method. The appeal of LBM lies in its local, linear calculations, allowing for optimal parallel calculations. For further details on LBM or SBB, refer to Aidun *et al.* (1998) and Aidun & Clausen (2010).

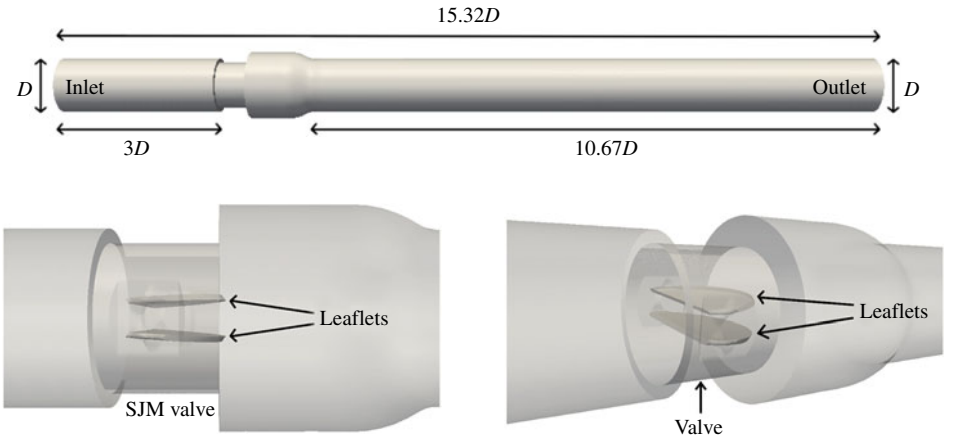

FIGURE 2. Computational model of the experimental *in vitro* flow loop.

The LBM is a direct numerical simulation (DNS) method for solving fluid flow and no special turbulence modelling is required. The method is normally applicable to low- to moderately-low-Reynolds-number flows. For higher-Reynolds-numbers, numerical instabilities arise and an entropic lattice-Boltzmann (ELB) method is used to eliminate these instabilities (Keating *et al.* 2007). These methods lead to stable explicit algorithms at low viscosities, allowing the modelling of very high Reynolds numbers with good accuracy. More details on ELB methods can be found in the paper by Keating *et al.* (2007).

2.2. *Numerical set-up and boundary conditions*

An *in vitro* pulsatile flow loop with an SJM valve in the aortic position is recreated computationally for use in the simulations (figure 2). A cardiac cycle with a period of 860 ms is modelled, with a mean flow rate of 4.5 l min^{-1}, a peak-flow rate of 25.0 l min^{-1}, and a forward flow duration of 300 ms. Blood is modelled computationally as an incompressible Newtonian fluid, with a kinematic viscosity matching whole human blood (3.5 cSt). The inlet and outlet lengths have a diameter of 25.4 mm. The valve is a 23 mm SJM valve with an inner diameter of 21.4 mm. Downstream of the valve on the aortic side is an axisymmetric expansion to a diameter of 31.75 mm representing the idealized aortic sinus root immediately downstream of the aortic valve. Figure 3 shows the ensemble-averaged flow rate and leaflet angle as they vary throughout the cardiac cycle. The Reynolds number at peak flow is 5780, with Reynolds number defined as $Re = U_{avg}D/\nu$, where D is inlet diameter, ν is kinematic viscosity and U_{avg} is the average inlet velocity. More descriptions of the set-up can be found in Dasi *et al.* (2007).

Simulations are performed with a spatiotemporal resolution of 80 μm and 2.4 μs per numerical timestep. The flow domain is discretized into a mesh of $4824 \times 408 \times 408$ grid nodes for the axial and cross-sectional directions, respectively. The spatial resolution is not high enough to resolve the hinge regions, but it is sufficient to resolve bulk flow through the valve. The very high temporal resolution allows for accurate direct modelling of unsteady non-periodic and turbulent flow at high Reynolds numbers with small time scales. Although the fluid domain employs uniform 3D grid spacing with no near-wall clustering, the resolution of the simulations

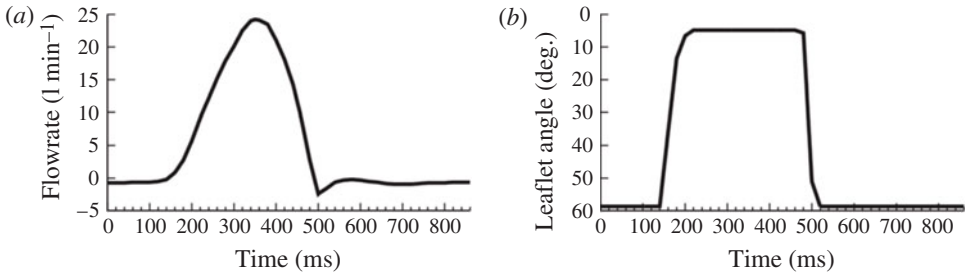

FIGURE 3. Flowrate and leaflet angle variation for one cardiac cycle: (*a*) flowrate curve; (*b*) leaflet angle curve.

is sufficiently high to accurately resolve the solid boundaries for both the valve housing and the leaflets.

At the inlet of the domain (ventricular side), a plug flow profile is prescribed based on the time-varying flowrate curve data (figure 3*a*). Plug flow is chosen owing to the high Womersley number of this flow ($Wn = 18$). At the outlet of the domain (aortic side), a stress-free boundary condition is applied. The flowrate inlet and stress-free outlet boundary conditions are applied as described by Aidun *et al.* (1998). During the diastolic phase when the flowrate becomes negative, the inlet and outlet boundary conditions are switched, allowing two-way pulsatile flow. Leaflet motion is prescribed throughout the cardiac cycle (figure 3*b*). Although translational motion does occur in real SJM valves, the simulations of this study restrict leaflets to rotational motion only. In these simulations, only one-way FSI is performed from the solid phase onto the fluid flow. Two-way FSI is possible with this numerical methodology, and the capability of this numerical method to model two-way FSI is discussed in Part 1 of this study (Yun *et al.* 2014*a*).

Parallel simulations are employed using 2592 processor cores, and one full cardiac cycle can be simulated with a run time of less than 20 h. However, this corresponds to 50 000 computational resource hours, and thus multiple cardiac cycles of simulation become very expensive. However, it has been shown (Yun *et al.* 2014*a*) that there is close periodicity in the flow fields with the simulation of just two cardiac cycles using this numerical method. Thus, the pulsatile flow simulations of this study only simulate two cardiac cycles.

For flow visualization, vortical structures are determined with 2D and 3D visualization. Pulsatile flow visualization is performed with greyscale 2D contour plots of out-of-plane vorticity magnitude at specific time points of the cardiac cycle. For 3D visualization, q-criterion is used to identify coherent vortical structures (Hunt, Wray & Moin 1988; Jeong & Hussain 1995). Uniformly coloured isosurfaces are shown when $q > 0$, where the vorticity rate dominates the strain rate and a coherent vortical structure is determined to exist. In some cases, the isosurface threshold is slightly increased to improve visualization and figures are marked by asterisks (*).

As shear stress on suspended blood elements is thought to contribute to haemolytic and thromboembolic complications, instantaneous plots of viscous fluid shear stress magnitude at perpendicular cutplanes are displayed throughout the cardiac cycle. The viscous shear stress for the 2D plane data is defined as

$$\tau_{xy} = \mu \left(\frac{\partial u}{\partial y} + \frac{\partial v}{\partial x} \right). \tag{2.1}$$

Age	Valve size (mm)	Systolic (%)	Heart rate (beats min^{-1})	Cardiac output (l min^{-1})	Peak flowrate (l min^{-1})	Peak *Re* number
18 years	21.4	40	70	5.0	25.0	5780
5 years	14	40	90	2.5	12.5	4418
6 months	9	50	120	1.25	4.8	2725

TABLE 1. Adult versus paediatric BMHV flow conditions.

Shear stress magnitude is given in dynes cm^{-2} as commonly used for BMHV flows, and contour plots of instantaneous viscous shear stresses are presented since blood damage is measured in terms of this actual shear stress (Dumont *et al.* 2007; Ge *et al.* 2008; Simon *et al.* 2010; Wu *et al.* 2011). For thromboembolic complications, these instantaneous shear stresses are combined with exposure time and used in a variety of damage accumulation models (Giersiepen *et al.* 1990; Tambasco & Steinman 2003; Dumont *et al.* 2007). These viscous shear stress plots are used here to characterize the flow field; however, future studies will employ suspended platelets for more accurate platelet damage quantification, as has been previously been performed with this numerical method (Wu *et al.* 2011).

BMHV flows with lower peak Reynolds numbers are also modelled for comparison, representing examples of physiologic flows through paediatric-sized prosthetic aortic valves. An example of a five-year-old child, with peak Reynolds number of $Re = 4418$, is modelled. An additional case of a six-month-old child, with peak Reynolds number of $Re = 2725$, is also modelled. The flowrate and leaflet motion variation of these two alternative flows are scaled from adult flow conditions, as experimental data of these paediatric BMHV flows do not exist. The comparison of simulation conditions are given in table 1, with the paediatric flow conditions selected from within pre-implantation ranges given in the literature (Sluysmans & Colan 2005; Zilberman, Khoury & Kimball 2005; Kaldararova *et al.* 2007; Pettersen *et al.* 2008; Pees *et al.* 2013; Yoganathan *et al.* 2013). Final paediatric flow conditions are selected as typical physiological values (table 1) within these ranges after consultation with Dr Doff McElhinney of NYU Langone Medical Center and clinicians from Children's Hospital of Philadelphia and Children's Healthcare of Atlanta. These simulations demonstrate variation of BMHV flows across different physiological conditions. More details of the set-up of these simulations can be found in the literature (Yun 2014; Yun *et al.* 2014*b*).

3. Results

3.1. *Pulsatile flow visualization: key timepoints*

For timepoints throughout the cardiac cycle, figures 4–8 all use the same out-of-plane vorticity contour scaling as shown in figure 4(*a*).

For leaflet opening with $Re \approx 0$, two vortex wakes are shown to form at the points where the leaflet tips separate from the valve housing (figure 4). In addition, it is noted that the leaflet opening seems to push fluid upstream in the b-datum line, causing its own wake. This is also apparent from the 3D view, where coherent vortical structures are noted at the leaflet edges as well as at the b-datum rectangular plane. Moderately high instantaneous shear stresses are seen from these leaflet opening wakes as well, with very low shear stress values throughout the rest of the flow field.

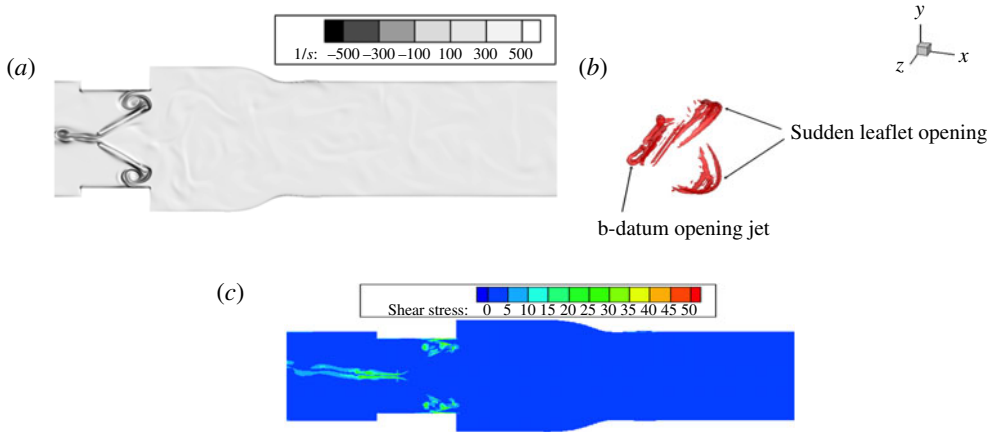

FIGURE 4. Opening phase: (*a*) 2D vorticity, (*b*) 3D *Q*-criterion isosurfaces and (*c*) viscous shear stresses.

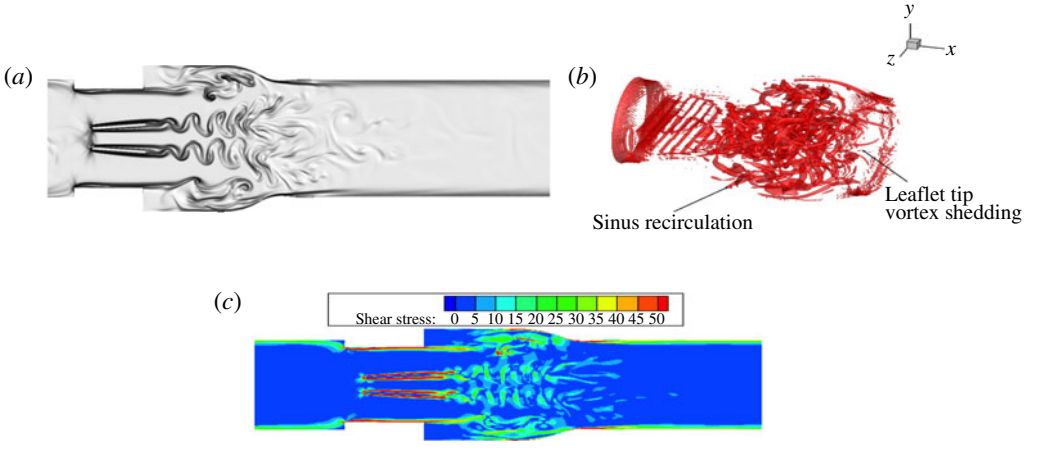

FIGURE 5. Acceleration phase: (*a*) 2D vorticity, (*b*) 3D *Q*-criterion isosurfaces* and (*c*) viscous shear stresses.

During the acceleration phase ($Re = 2070$), the flow is characterized primarily by the two von Kármán vortex streets past the two leaflet tips (figure 5). The sinus expansion region also contains two recirculation zones caused by the increased expansion volume and the vortex shedding past the sudden step into the sinus expansion. This flow is still considered laminar during this mid-acceleration phase, with the vortex structures very organized and repeatable in similarity from cycle to cycle. The 3D visualization highlights the three-dimensionality of this vortex shedding and recirculation.

It is observed that the highest fluid shear stresses during this instantaneous forward flow point are near the leaflet surfaces. This high-shear region is maintained very close to the leaflet surface, however, with no flow separation until the vortex shedding past the ending leaflet tips. Another high-shear region is observed owing to the sharp contraction into the valve region, although this is also maintained close to the surface of the valve housing. It is noted that although there are coherent von Kármán vortex

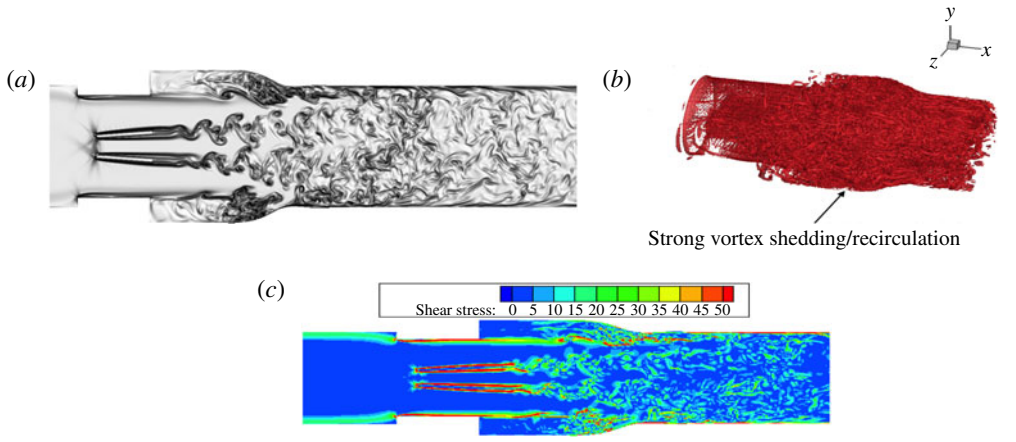

FIGURE 6. Peak flow: (*a*) 2D vorticity, (*b*) 3D *Q*-criterion isosurfaces and (*c*) viscous shear stresses.

streets in flow past the open leaflets, these vortex streets do not exhibit very high instantaneous shear stresses values.

At peak flow ($Re = 5780$) in figure 6, the primary features of vortex shedding past the leaflet tips and sinus step are noted to be similar to accelerating flow. However, the flow field becomes more disorganized and chaotic owing to the maximum Reynolds number achieved by this flow. The higher-resolution simulation shows the breakup of the coherent von Kármán vortices into smaller and smaller eddies as the flow becomes more disorganized and chaotic. The 3D visualization shows the entire domain to be filled with coherent vortical structures.

The viscous shear stress plots again demonstrate high-shear regions close to the leaflet surfaces and the valve housing. Although the flow past the leaflet tips include small scale, disorganized eddies, the instantaneous fluid shear stresses in these regions are only moderately high. Higher shear stresses are noted instead in the sinus expansion region, where flow recirculates owing to the sudden expansion step. The vortical structures begin dissipating as they propagate further downstream on the aortic side. Far downstream of the sinus region, lower instantaneous shear stress values are also observed.

Figure 7 shows the sudden closing of the leaflets with reverse flow ($Re = 580$ in reverse flow). Two leaflet closing leakage jets are formed at the instant the leaflet tips touch the valve housing. In addition, owing to the sudden reduction of the central orifice area as well as reverse flow, a leakage jet squeezes in the upstream direction at the b-datum line. Owing to the reduced flow rate and viscous dissipation, vortex washout occurs downstream of the valve, shown by neutral grey contours. This is in comparison with the stronger vorticity in accelerating flow, which is depicted by stronger black and white contours.

The viscous shear stress plots demonstrate higher instantaneous shear stresses right at the leaflet closing wakes and particularly at the central b-datum leakage jet. However, the flow downstream of the valve shows both vortex washout (figure 7*a*) and lower shear stress values (figure 7*c*).

In the mid-diastole phase, there is significant vortex washout in the aortic side and reverse leakage flow in the b-datum plane (figure 8). During mid-diastole, the reduced b-datum orifice area results in a strong leakage jet in the upstream direction. This

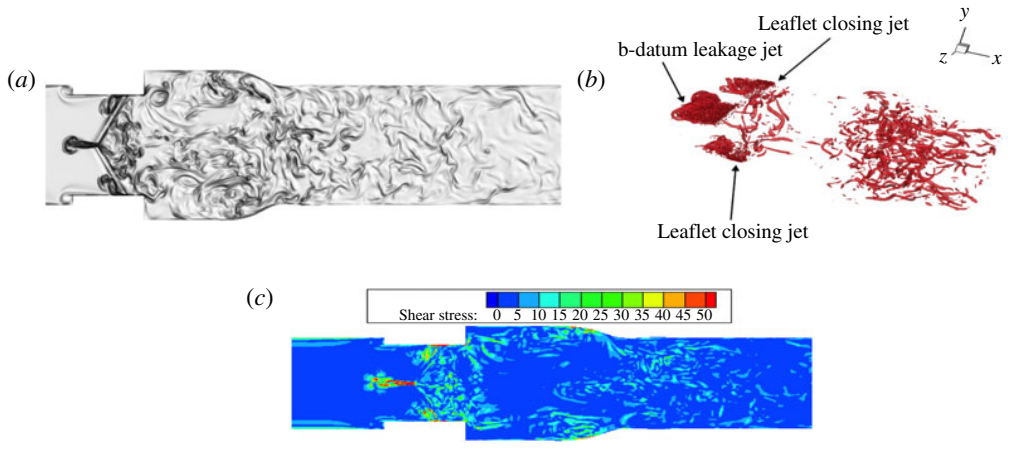

FIGURE 7. Closing phase: (*a*) 2D vorticity, (*b*) 3D *Q*-criterion isosurfaces* and (*c*) viscous shear stresses.

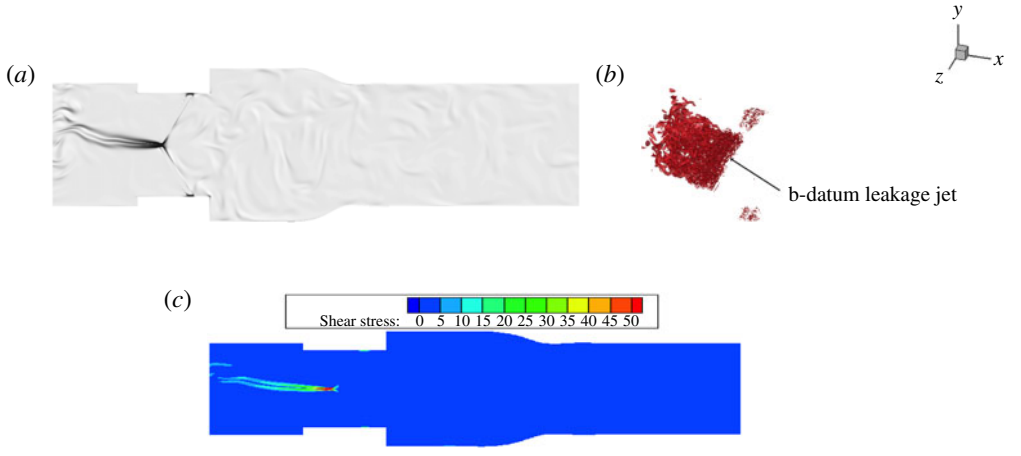

FIGURE 8. Leakage phase: (*a*) 2D vorticity, (*b*) 3D *Q*-criterion isosurfaces and (*c*) viscous shear stresses.

was not captured by previous numerical studies that simulate zero flow in place of reverse leakage flows for full cardiac cycle simulations. It is also noted that viscous dissipation has caused a significant vortex washout downstream of the valve. In the 3D visualization, the only coherent structures are from the strong b-datum leakage jet in the upstream direction. The vortex washout downstream of the valve has dissipated any coherent vortical structures, and thus none are shown. It is noted that during mid-diastole, the b-datum leakage jet is shown to oscillate in direction but prefers one direction over time, as illustrated in figure 8 with a top-leaning leakage jet. The viscous shear stress field shows very low instantaneous shear stresses throughout the domain, with the exception of the b-datum leakage jet.

3.2. *Accelerating to peak flow*

The simulations are performed at uniform high spatiotemporal resolution, which is able to capture small-scale structures throughout the entire domain. This is particularly

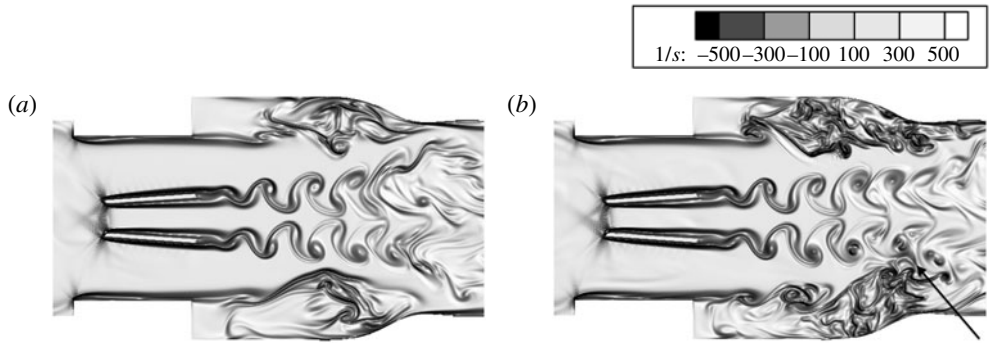

FIGURE 9. High accelerating flow with coherent vortical structures in flow past leaflet tips, with mixing of leaflet vortex wakes and sinus recirculation region: (*a*) $Re = 4400$; (*b*) timepoint 15 ms later.

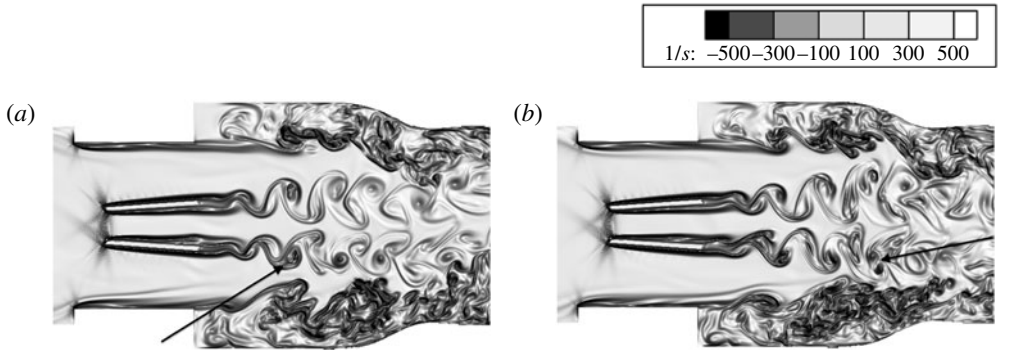

FIGURE 10. Peak flow with coherent vortical structures breaking into small-scale eddies: (*a*) $Re = 5700$; (*b*) timepoint 6 ms later.

observed for the flow past the leaflet tips, where the coherent vortical structures of accelerating flow are broken into small-scale eddies at peak flow. The images in this section use the same vorticity contour scaling for all plots. At high accelerating flow ($Re = 4400$), coherent vortical structures are still observed past the leaflet tips (figure 9*a*). At a timepoint only 15 ms later, some interaction begins between the leaflet tip vortices and the recirculating region of the sinus expansion (figure 9*b*). It is noted that the vortex shedding past the leaflet tips is still coherent, but the recirculation region becomes more disorganized and larger, thus causing a mixing with von Kármán vortex streets.

Near-peak-flow with $Re = 5700$, an initial vortex is shed from the leaflet tips (figure 10*a*). Here the vortex is coherent and unmixed with the sinus expansion recirculation region. Just 6 ms later at peak flow (figure 10*b*), this vortex is broken into two small-scale eddies. This is captured by the high spatial resolution simulations for the entire flow domain, whereas other numerical methods concentrate high resolution at only the valve region. This highlights the importance of modelling high resolution throughout the flow domain, as important small-scale features would not be captured otherwise.

When the flowrate decelerates but is still near peak flow ($Re = 5600$), two small-scale eddies are formed from coherent vortical shedding past the leaflet

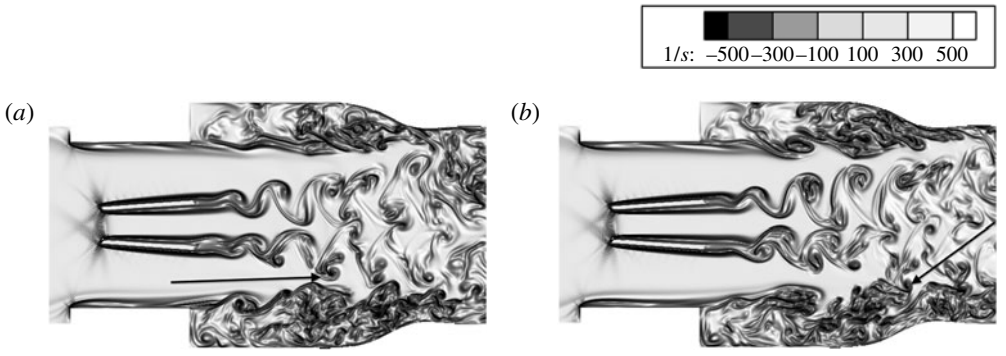

FIGURE 11. Small-scale eddies interacting with sinus expansion recirculation: (*a*) $Re = 5600$, deceleration phase; (*b*) timepoint 7 ms later.

tips (figure 11*a*). This leaflet tip vortex shedding spreads throughout the sinus expansion further downstream of the valve as smaller eddies are formed. At this higher-Reynolds-number flow, the sinus recirculation region is also shown to be very strong and mixes with leaflet tip vortices only 7 ms later. These figures demonstrate the complex interaction of the vortex shedding past the leaflet tips with the strong recirculation region caused by the sudden sinus expansion step.

The differences in fluid shear stress magnitudes between early accelerating ($Re = 2070$) and peak flow ($Re = 5780$) are detailed in figure 12. Immediately downstream of the leaflet tips (figure 12*a*), the fluid stresses at a perpendicular line are very similar between accelerating and peak flow. This shows maximum peaks representing immediate vortex shedding past the leaflet tips, as well as two additional peaks from flow past the sudden sinus expansion step. At this location, the vortices are immediately shed from the leaflets and have not had a chance to break up into smaller eddies in the case of peak flow, thus resulting in similar shear stress profiles.

A distance 10 mm downstream of the leaflets (figure 12*b*), the two flow regimes show greater differences in fluid stresses. For peak flow, the shear stresses are higher in peak magnitudes (at the leaflet vortex shedding and sinus expansion step) and also show high fluctuations. This is likely owing to the more chaotic and disorganized flow downstream of the leaflets, where the coherent vortices break into smaller scale eddies for peak flow. Thus, owing to presence of smaller scale vortices downstream of the leaflets, the shear stress variation is higher for peak flow.

Finally, 20 mm downstream of the leaflets but still within the sinus region (figure 12*c*), the shear stress profiles are drastically different. The peak-flow profile shows high fluctuations in shear stresses, particularly in the sinus region where the strong recirculation regions are observed. This high fluctuation is also observed in the centre of the domain, again representing the unsteady fluctuation in shear stresses owing to the smaller-scale eddies that are present for peak flow. It is important to note, however, that the overall magnitudes of shear stresses decrease further downstream of the leaflets despite the high fluctuations. It is also important to highlight that these fluctuations are observed quantitatively (in addition to previous qualitative observations in the vorticity plots) significantly downstream of the valve region. Thus, high spatial resolution is needed beyond just the valve region, as the important small-scale flow features and shear stress fluctuations are found downstream of the valve.

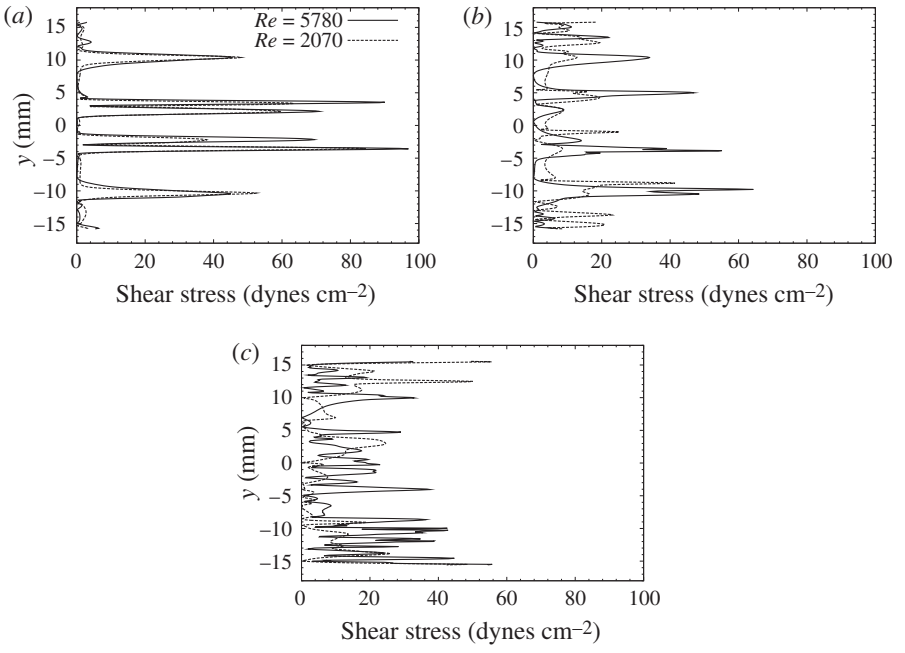

FIGURE 12. Comparison of viscous fluid shear stresses at perpendicular lines downstream of the leaflet tips for accelerating and peak flow: (*a*) $x = 2.0$ mm; (*b*) $x = 10.0$ mm; (*c*) $x = 20.0$ mm.

3.3. *Leaflet closing*

The numerical simulations of this study are able to capture the closing leaflet phase without any contact modelling problems between the leaflet and valve housing. The ventricular upstream is four diameters in length and is sufficient for the interior flow field to not be affected by the outflow boundary condition. Previous studies have not concentrated on capturing the complex dynamics of sudden leaflet closing, as well as leaflet–valve impact.

At the beginning of sudden leaflet closing, many of the vortical structures on the aortic side begin to dissipate and closing leaflet wakes begin to form (figure 13). The remnants of forward flow past the leaflet tips are shown as a weak vortex trail in the sinus expansion. The shear stress plot also demonstrates low and moderate instantaneous shear stresses in the aortic downstream region with some higher shear stresses in the sinus expansion. High instantaneous shear stress values are observed at the leaflet tips caused by the rapid leaflet motion.

At a timepoint 10 ms later, the leaflet rapid motion causes vortex shedding in its wake, as shown in figure 14. This leaflet wake also shows a trail vortex wake in the sinus expansion caused by the remnants of vortex shedding past the leaflet. These two coherent closing wake vortices are also highlighted by strong instantaneous shear stresses near the leaflet tips. Downstream of the valve, the shear stress field shows very low stress values as caused by viscous dissipation and the low overall flowrate.

Leaflet closing impact with the valve housing shows very interesting flow features as well. The initial impact between the leaflets and valve housing (figure 15*a*) results in leaflet closing wakes along the valve housing surface. In addition, a noticeable squeezing jet is observed owing to the reduction of the central orifice area. This

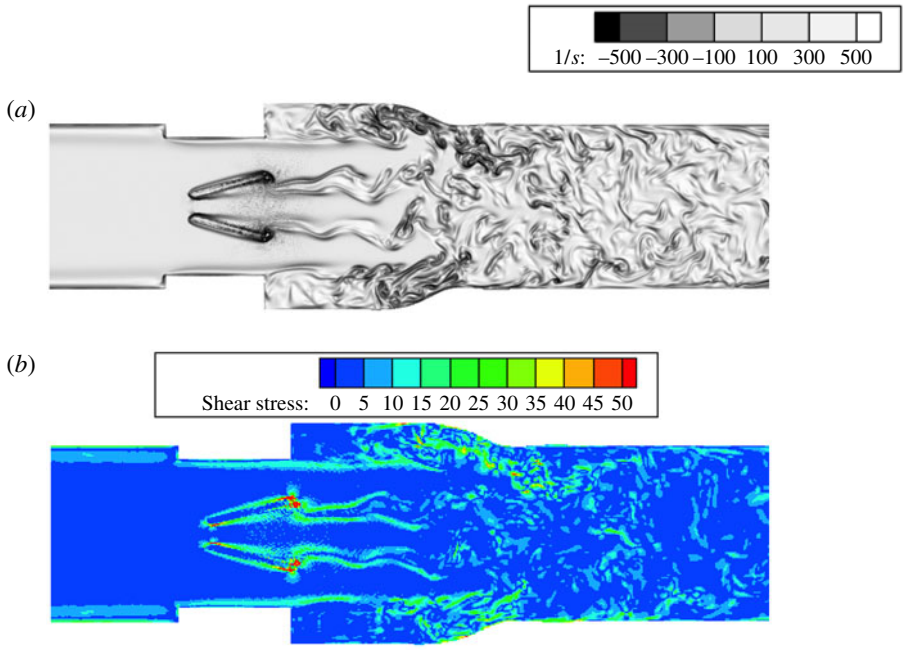

FIGURE 13. Vorticity and shear stress field (dynes cm^{-2}) plots at beginning of closing phase with sudden leaflet motion and initial closing wakes: (*a*) 2D vorticity; (*b*) viscous shear stress (dynes cm^{-2}).

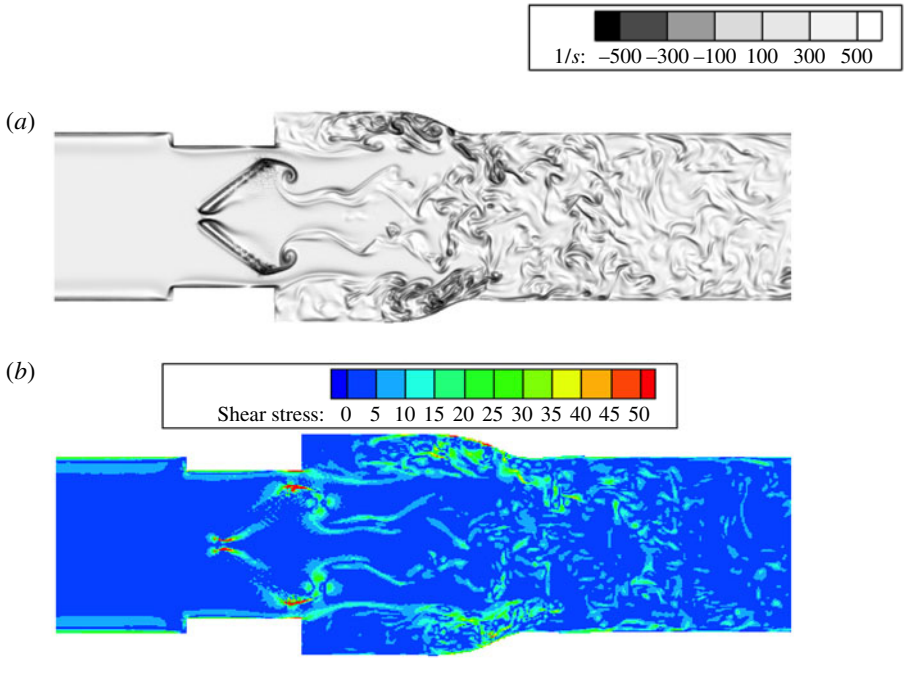

FIGURE 14. Vorticity and shear stress (dynes cm^{-2}) field plots at rapid leaflet closing phase with strong leaflet closing vortex wakes: (*a*) 2D vorticity; (*b*) viscous shear stress (dynes cm^{-2}).

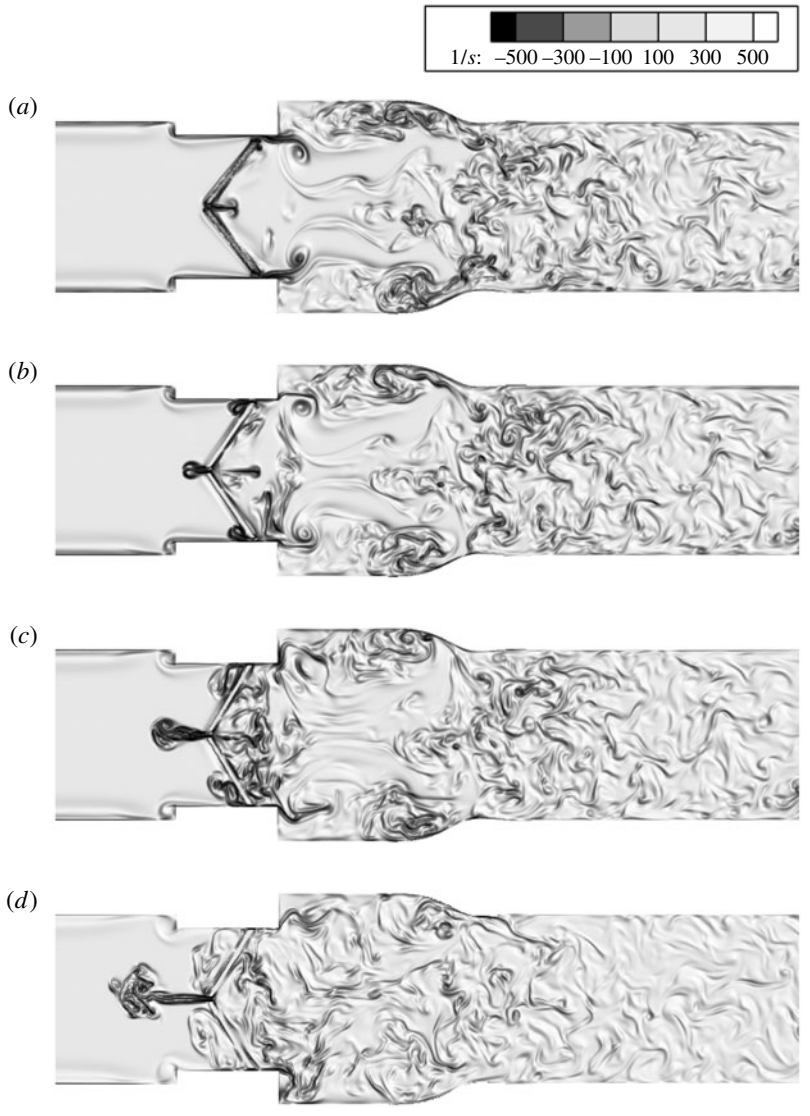

FIGURE 15. Vorticity plots upon leaflet closing impact with valve housing. (*a*) Leaflets: initial closing impact. (*b*) Generation of triple leakage jets. (*c*) Growth of triple leakage jets. (*d*) Coherent b-datum jet with vorticity washout in the rest of the domain.

squeezing jet is initially directed in the aortic side of the valve. The downstream region is characterized by rapidly dissipating flow structures at the onset of diastole.

Then 10 ms afterwards, the initial formation of three leakage jets is observed, which are caused by the leaflet–valve housing impact as well as the b-datum central orifice (figure 15*b*). These three jets are formed on the ventricular side of the valve, and fluid is shown to squeeze in these small gaps. The initial impact causes a central jet on both the ventricular and aortic side as the leaflets have rapidly closed. At this timepoint, vortical structures are shown to form directly downstream of the valve owing to leaflet–valve impact.

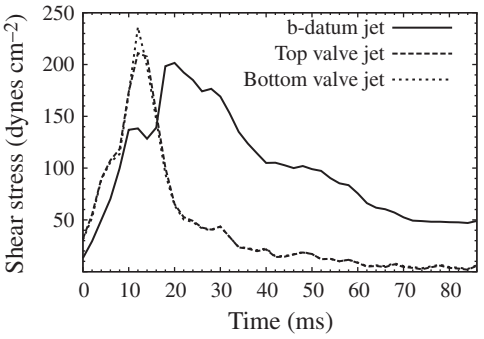

FIGURE 16. Shear stress (dynes cm^{-2}) at various leakage jets upon leaflet closing impact.

A stronger b-datum jet advects towards the ventricular side centrally after an additional 10 ms (figure 15*c*), although the tip of this structure grows in size. Also noticeable is the growth of vortical structures on the immediate aortic side of the leaflets, caused by the sudden leaflet impact with the valve. Figure 15(*d*) shows a timepoint 20 ms later, with a washout of vortical structures throughout the flow domain. However, it is noted that the b-datum central jet is still coherent and advects centrally upstream, spreading outwards throughout the ventricular side.

The simulations of this study are also able to resolve leakage jets for both the central b-datum jet and the circular gap between the leaflets and the valve housing. The b-datum gap is estimated at 0.76 mm and the valve-housing gap is estimated at 0.336 mm. The instantaneous shear stresses are averaged for fluid nodes across these gap regions and are plotted in figure 16.

The shear stress variation upon leaflet closing impact is very similar for both the top and bottom leaflet–valve impact jets. In addition, the peak value of shear stress across this gap is comparable with the peak value of shear stress for the central b-datum jet. It is interesting to note that the maximum shear stress occurs for the central jet approximately 10 ms after the timepoint for maximum shear stress for the leaflet–valve jets. The shear stress rise to maximum value is slightly slower for the central leakage jet, despite the gap reduction occurring simultaneously with leaflet–valve impact.

It is also shown that upon initial impact, the shear stress levels rise to a maximum value and then steadily decrease during the early part of the diastolic reverse flow phase. However, the shear stress magnitude for the b-datum jet drops slowly as compared with the rapid decrease in stress values for the leaflet–valve leakage jets. It is shown in the next subsection that this drop in shear stresses precedes a mid-diastolic leakage flow through these same gaps.

3.4. *Diastole*

Diastole begins upon the reverse flow phase, which includes the previously discussed closing impact phase. However, this impact phase is considered early diastole, and is followed by a long time period (400 ms) of quasi-steady leakage flow, termed mid-diastole. Figure 17 shows axial velocity at the central b-datum jet and leaflet–valve jet for the entire diastolic phase, including both closing impact and mid-to-end diastole. The velocity is averaged across the gaps, as similarly performed in figure 16.

The axial velocity plot shows strong negative velocities at the leakage gaps upon leaflet impact. It is observed that the maximum negative velocity for the central jet

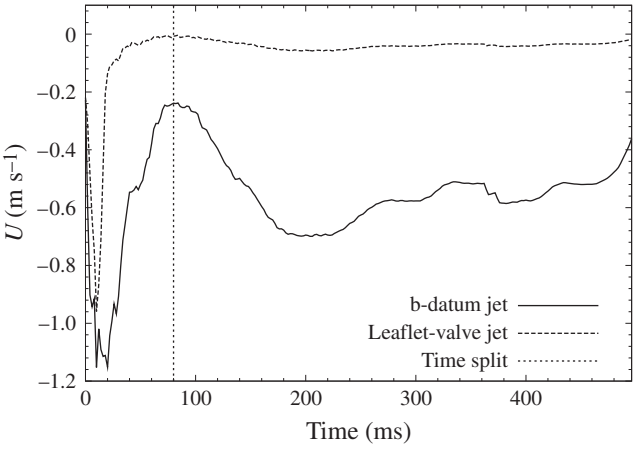

FIGURE 17. Axial velocity at leakage gaps for the reverse diastolic flow phase.

is larger than for the valve-housing leakage jets. A slight offset is again observed of 10 ms for the timepoint of maximum velocity, similar to the timepoint of maximum shear stress in figure 16. The rapid decrease in velocity after initial closing impact is observed for both leakage jets. However, it is seen that the decrease in leakage jet velocity is very rapid for the valve-housing leakage jet, with a near-zero reverse axial velocity 80 ms after initial impact.

The mid-diastolic flow phase is clearly demarcated by a time split line in figure 17. After the sudden reduction in reverse axial velocity, the mid-diastolic leakage phase leads to a secondary reverse flow. This reverse flow is not as strong as for initial impact, but lasts for over 400 ms during diastole. For the leaflet–valve gaps, the reverse axial velocity is quasi-steady but with magnitudes close to zero.

The central b-datum plane is rectangular and approximately 13.35 mm^2 in area. Thus, the maximum leakage flowrate through the central jet can be approximated (based on area times average velocity) as 15.35 $cm^3\ s^{-1}$, or 0.921 15 l min^{-1}. The leaflet–valve gap is circular and approximately 11.17 mm^2 in area. The maximum leakage flowrate through this gap can be approximated as 10.71 $cm^3\ s^{-1}$, or 0.642 66 l min^{-1}. The hinge regions are not resolved spatially with an 80 μm resolution and thus these leakage gaps cannot be captured. The total maximum leakage flowrate is thus calculated at 1.56 l min^{-1}, although it is noted that the prescribed maximum leakage flowrate from experimental data is 2.4 l min^{-1}. It is important to note, however, that these calculations are performed assuming average leakage gap velocity applies throughout the entire gap area, and is thus an approximation.

For shear stress variation for the diastolic flow phase, the initial closing impact leads to high shear stresses across the various leakage gaps that rapidly decrease after 80 ms (figure 18). Similar to the axial velocity variation (figure 17), a clear time demarcation can be made between early diastolic impact and the quasi-steady mid-diastolic flow phase.

Once again, as in the axial velocity variation, the shear stress values for mid-diastole do not reach the maximum levels as in closing impact. However, the moderate levels of shear stress for the b-datum jet are maintained for over 400 ms of diastole. It is observed that the b-datum jet shear stresses are significantly larger than for the leaflet–valve gaps. This has implications on potential platelet damage in leakage flow through this central gap.

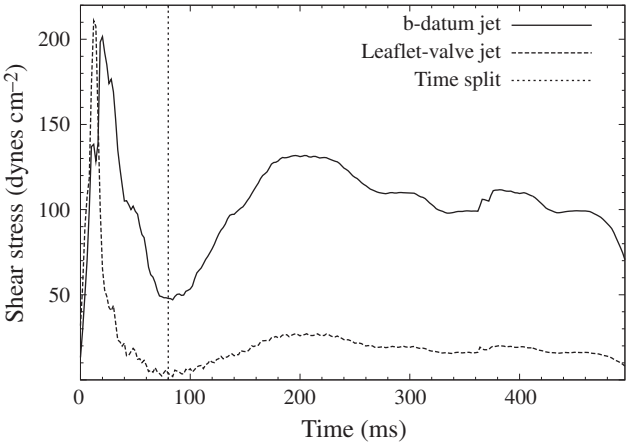

FIGURE 18. Shear stress magnitude at leakage gaps for reverse diastolic flow phase.

Figure 19 shows vorticity contours at various instantaneous timepoints throughout mid-diastole. These images are taken from multiple cardiac cycles and illustrate that the mid-diastolic leakage jet can vary in direction of flow. Figure 19(*b–d*) employ the same contour scaling but different lighting to highlight certain flow features. Figure 19(*a*) shows a more centrally flowing b-datum jet with no large-scale vortical structures shown besides the b-datum leakage jet. Figure 19(*b*) shows the diastolic leakage jet mixing with large scale vortices on the bottom half of the ventricular side (backlighting slightly modified). This is in contrast to figure 8 with a top-leaning jet. Figure 19(*c*,*d*) both show the unorganized flow on the ventricular side during diastole, with an obvious lack of symmetry in the vorticity field. In these two figures, a small b-datum leakage jet shows a slight preferential direction that corresponds with the side that shows stronger vortical structures. This preferential direction is observed even before interaction between the leakage jet and the vortical structures, and this asymmetry in the leakage jet will be explored in the discussion section (§ 4).

3.5. *Turbulent flow features*

The simulations of this study are validated against experimental results in Part 1 of this study (Yun *et al.* 2014*a*). For quantitative validation of pulsatile flow, 200 time samples are taken within the integral time scale of peak flow when comparing to mean flow data from experiments, as simulating 200 cardiac cycles is not possible owing to computational resource constraints. This same methodology of taking samples within the peak flow integral time scale is employed to characterize turbulence in this flow. The integral time scale at peak flow is 58.7 ms. Thus, 200 time samples of the flow field are taken in a 25 ms time period to detail the turbulent features of peak flow, which is of the same order of the integral time scale. From these time samples, the mean velocity flow field is first computed and the fluctuating turbulent velocity fields are then computed for each of the 200 time samples.

The rate of dissipation of turbulent kinetic energy (TKE), ϵ, is calculated for the peak-flow phase of the cardiac cycle. From TKE equations, this rate is defined as

$$\epsilon = 2\nu\overline{s_{ij}s_{ij}} \tag{3.1}$$

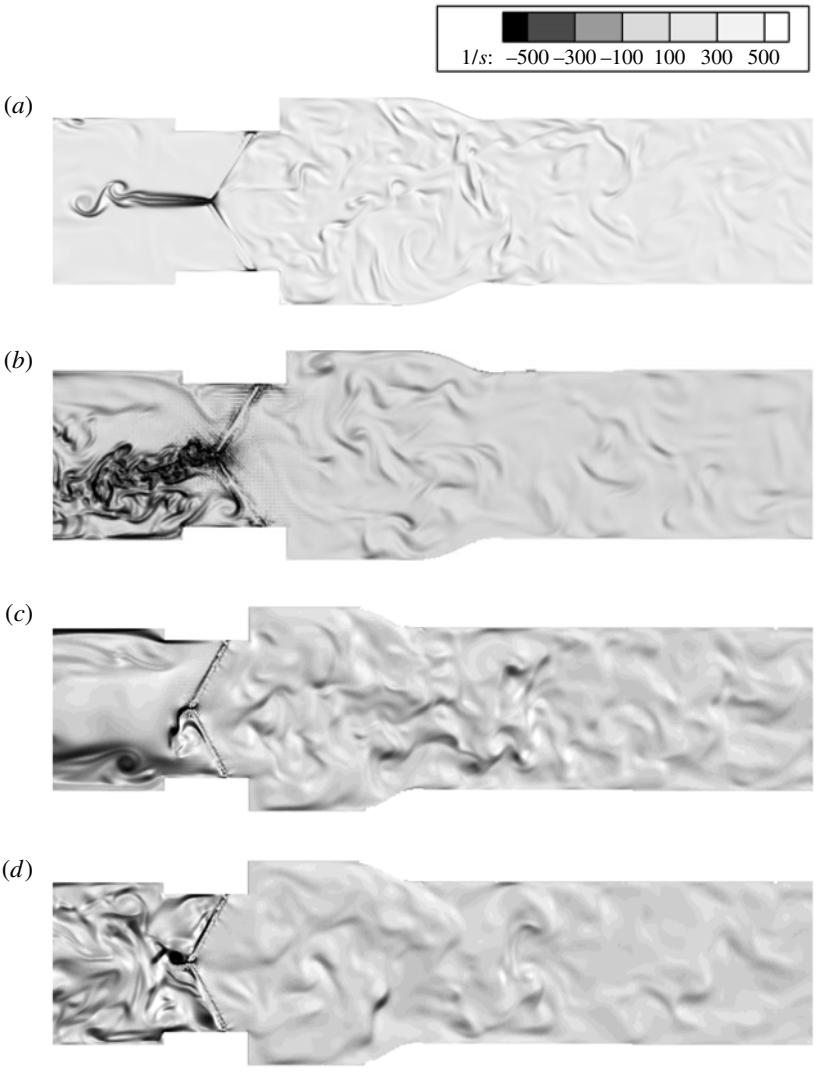

FIGURE 19. Demonstration of variation of b-datum leakage jet direction. Vorticity magnitude scaling identical for all plots. (*a*) Central b-datum jet. (*b*) Asymmetry towards the bottom side. (*c*) Slight asymmetry towards the bottom side. (*d*) Slight asymmetry towards the top side.

where s_{ij} is the rate of strain tensor of the turbulent fluctuating velocity field (u', v', w'), and $\overline{(\,)}$ denotes time averaging. As the components of s_{ij} include 3D velocity gradients, a 3D flow field is technically required. Thus, an additional 200 time samples are taken at the same simulation timepoints but from a 2D perpendicular flow field cutplane that is one grid spacing apart in the depth (z) direction. This creates a thin 3D flow field of data, allowing the computation of the full 3D velocity gradient tensor and thus the calculation of the TKE dissipation rate, ϵ.

In the case of experiments where only 2D plane data and measurements are possible, the rate of TKE dissipation is sometimes approximated by assuming local isotropy

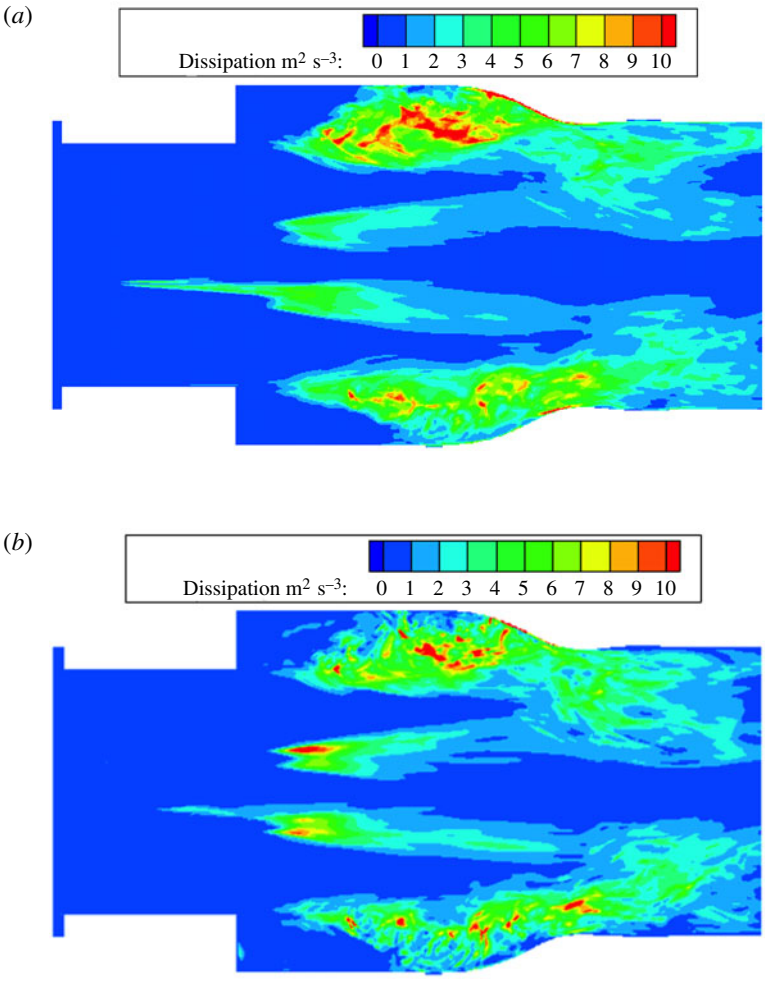

FIGURE 20. TKE rate of dissipation contour plots for 2D perpendicular plane at peak flow using TKE equation (ϵ) and local isotropy (ϵ_{iso}) methods. (*a*) Dissipation rate, ϵ, from the TKE equation. (*b*) Dissipation rate, ϵ_{iso}, assuming local isotropy.

(Brown, Parsheh & Aidun 2006; Ge *et al.* 2008). This approximation is given by

$$\epsilon_{iso} = 15\nu\overline{\left(\frac{\partial u'}{\partial x}\right)^2}. \tag{3.2}$$

These two methods are employed and their results are compared, both to determine turbulent energy dissipation rate and to evaluate the validity of the local isotropy approximation ϵ_{iso} for this specific BMHV flow. 2D contour plots of ϵ and ϵ_{iso} are calculated by the two methods for 200 time samples (figure 20). Qualitatively the two fields are similar with high dissipation rates observed in the top sinus region. The local isotropy approximation method also shows a higher peak dissipation rate for vortex shedding past the top leaflet.

It is observed that the dissipation rate plot is not symmetric about the centreline, despite the averaging of 200 time samples. This can be explained by the nature of

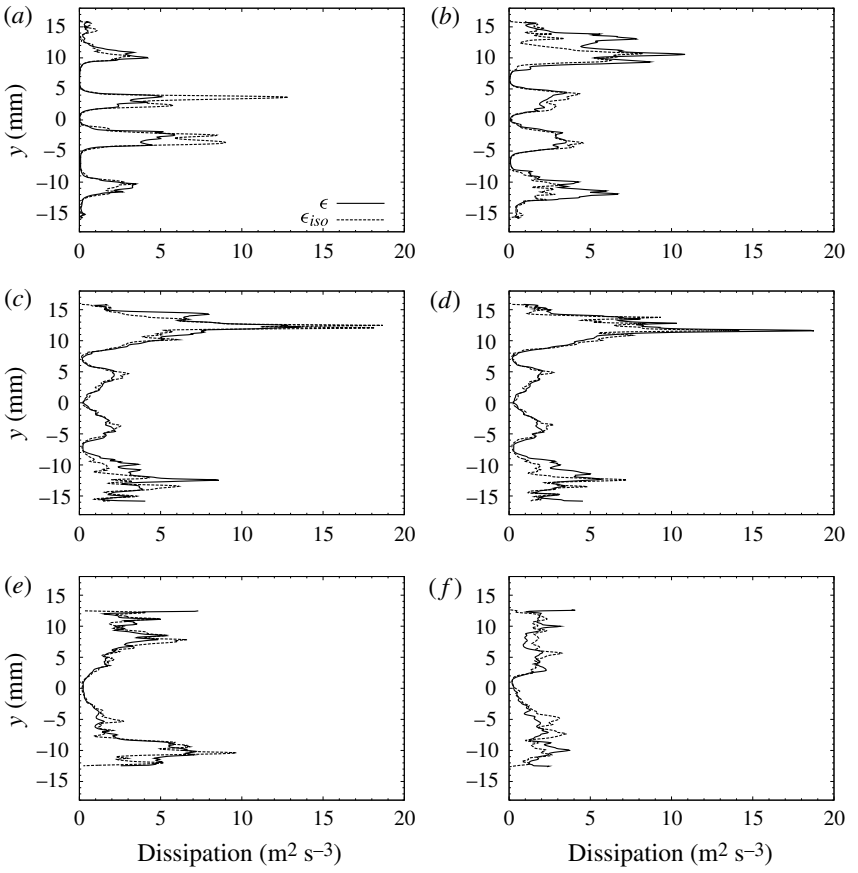

FIGURE 21. TKE rate of dissipation line plots at peak-flow, calculated from TKE equation (ϵ) and local isotropy approximation (ϵ_{iso}): (*a*) $x = 5.0$ mm; (*b*) $x = 10.0$ mm; (*c*) $x = 16.0$ mm; (*d*) $x = 17.0$ mm; (*e*) $x = 30.0$ mm; (*f*) $x = 40.0$ mm.

time averaging that is employed for the dissipation rate plot, where time samples are taken from pulsatile flow within a small range of 25 ms. This time period is important because it is on the same order of the integral time scale of peak flow (58.7 ms), but also within a window of minimal flowrate variation (max variation 1.2 %) at peak flow. However, there are natural asymmetries of leaflet vortex shedding at peak flow. These wake vortices do not have sufficient time to shed, develop, and dissipate within this averaging time frame. Thus, some degree of asymmetry in the contour fields of ϵ and ϵ_{iso} are expected.

The two dissipation rate calculation methods are also compared at perpendicular lines downstream of the leaflets. At a distance 5 mm downstream of the leaflets (figure 21*a*), the two methods show similar dissipation rates in the sinus expansion regions. However, the local isotropy approximation method computes a significantly higher maximum dissipation rate for flow past the leaflets ($\epsilon_{iso} = 12.85$ m^2 s^{-3}) compared with the 3D TKE equation definition ($\epsilon = 5.87$ m^2 s^{-3}). A distance 10 mm downstream of the leaflets (figure 21*b*), the dissipation rates are similar both in shape and in magnitudes.

The dissipation rate is highest in the sinus expansion region, at 16–17 mm downstream of the leaflets for both methods (figure 21*c*,*d*). This occurs at slightly

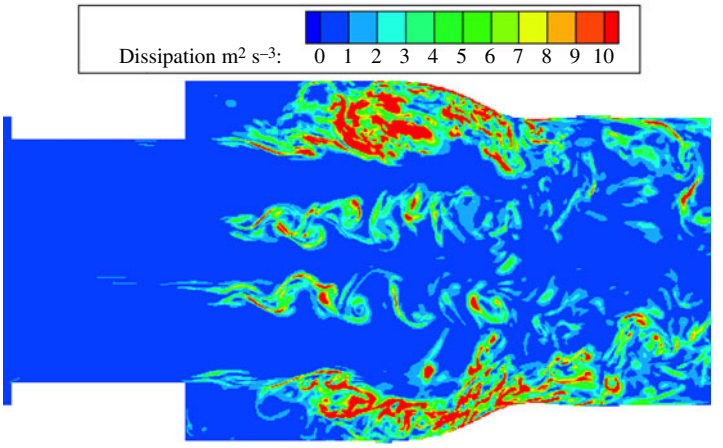

FIGURE 22. Instantaneous turbulent energy dissipation rate, ϵ_{inst}, at peak flow.

different axial positions, but the magnitudes of maximum dissipation rate are similar (18 m^2 s^{-3}). Further downstream of the leaflets (30 and 40 mm), the two methods show similar profiles both qualitatively and in magnitudes (figure 21*e*,*f*).

It is determined that for comparisons at perpendicular lines downstream of the leaflets, the two methods are similar in profile and magnitude of dissipation rates for peak flow. The only major difference is observed 5 mm downstream of the leaflets (figure 21*a*), where the dissipation rate downstream of the leaflets is significantly higher for the local isotropy approximation ϵ_{iso} method. Goodness-of-fit R^2 analysis is performed for comparisons of ϵ and ϵ_{iso} at these perpendicular lines. This analysis results in R^2 values varying from 0.813 to 0.914 for perpendicular lines, with one notable exception at 5 mm downstream of the leaflets where $R^2 = 0.503$. Other than this discrepancy, the assumption of local isotropy in order to calculate turbulent energy dissipation rates is shown to be a good approximation.

The instantaneous turbulent energy dissipation rate can be calculated for peak flow as well (figure 22), and is defined as

$$\epsilon_{inst} = 2\nu s_{ij} s_{ij} \tag{3.3}$$

compared with the mean dissipation rate contour plots (figure 20), high instantaneous dissipation rates are observed throughout the flow field, particularly for the sinus recirculation and leaflet wake regions. This also demonstrates the high fluctuations present in these regions and the high potential for turbulence in this flow, particularly for the peak-flow phase.

The Kolmogorov scale is calculated from the mean dissipation rate as

$$\eta = \left(\frac{\nu^3}{\epsilon}\right)^{1/4}. \tag{3.4}$$

For the sinus expansion, the peak dissipation rates correspond to Kolmogorov lengths of approximately 40–42 μm in the recirculation region. For flow past the leaflet tips, the definition from the TKE equation yields a Kolmogorov length of approximately 52 μm. From the local isotropy approximation, the Kolmogorov length is approximated as 43 μm. As the spatial resolution of these simulations is 80 μm, the smallest Kolmogorov lengths are not being resolved by the numerical simulations.

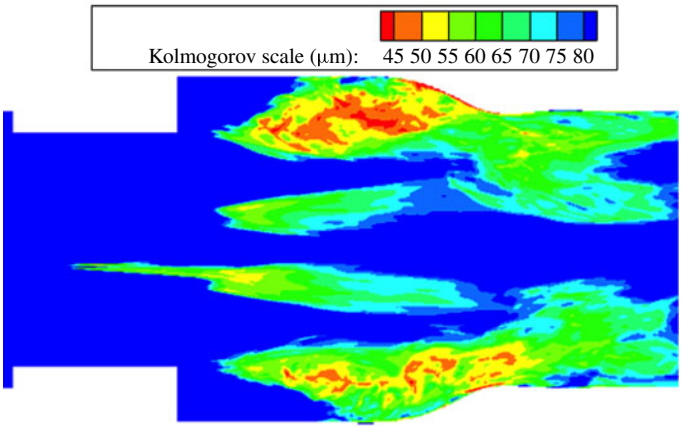

FIGURE 23. Contour plot of Kolmogorov spatial scales (η) based on mean dissipation rates, with contour scaling capped at 80 μm.

However, it should be noted that the Kolmogorov scales are not a strict threshold but represent an order of magnitude of the smallest eddy scales.

The Kolmogorov spatial scales can be estimated throughout the central plane of the flow (figure 23) based on the calculated mean dissipation rates ϵ at each point and (3.4). This demonstrates that most of the flow field is being resolved by the high spatial resolution of these simulations at 80 μm. The lowest scale is in the top sinus region, with a Kolmogorov length of approximately 40 μm. Although this again means that the simulations technically under-resolve the Kolmogorov scale, the spatial resolution is within two times the lowest Kolmogorov length scale. Thus, the numerical simulations are still able resolve the lower-order moments of the turbulent flow (Yeung & Pope 1989; Pope 2000).

Energy spectra can also be plotted against wavenumber for peak flow to determine the existence of turbulence in this BMHV flow (figure 24). This spectra is generated for wavenumber κ_1, corresponding to the streamwise axial direction. Sampling for this spectra is performed for 200 time samples spanning 25 ms. Sampling is also performed at multiple positions along the transverse (perpendicular to the leaflets) y-axis. This encompasses flow past the leaflets as well as the sinus recirculation region.

The spectra is generated for $E_{11}(\kappa_1)$, or energy for the streamwise turbulent velocity component, u'. Although BMHV flow is complex in its pulsatile nature and flow past two leaflets, it most resembles turbulent pipe flow. Thus, the streamwise velocity component and associated energy are chosen as most appropriate for the assumption of homogeneous flow for plotting energy spectra. The flow velocity in the transverse y direction is strongly affected by the presence of the two leaflets in BMHV flow, and thus energy is not computed for other velocity components. In classic turbulent channel and pipe flow problems as well, the transverse velocities are considered to not satisfy the condition of homogeneity (Kim, Moin & Moser 1987).

The plotted spectra (figure 24*a*) also shows the $-5/3$rd slope to demonstrate the presence of an inertial range and the presence of turbulence at peak flow. Although this inertial range contains some noise, a relatively good fit is shown with the $-5/3$rd slope for a range of wavenumber modes ($\kappa_1\eta = 0.004$–0.015). This shows the presence of turbulence at peak flow, despite the Reynolds number being relatively moderate ($Re = 5780$ at peak flow).

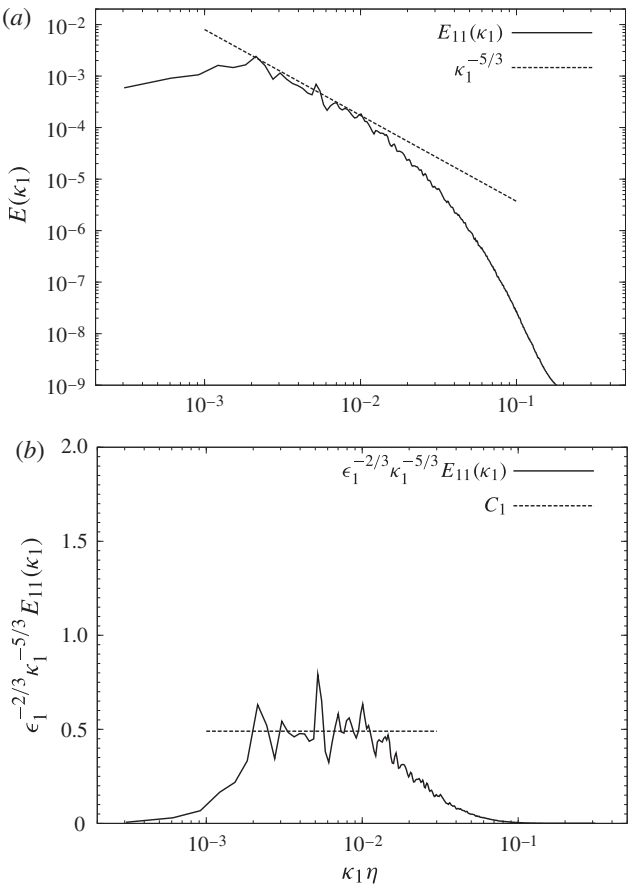

FIGURE 24. 1D energy spectra versus normalized wavenumber at peak flow: (*a*) 1D energy spectrum; (*b*) 1D compensated energy spectrum.

The compensated energy spectra is also plotted (figure 24*b*) along with the zero-slope constant C_1 line corresponding to the inertial range for 1D energy spectra, where $C_1 \approx 0.49$ (Pope 2000). Once again, this compensated spectra demonstrates noise in the inertial range but shows matching with the predicted C_1 line. A clear demonstration of turbulence in this pulsatile BMHV flow is not apparent, but these energy spectra show the development of a clear inertial range.

It is also observed that after the $-5/3$rd scaling for the inertial range, the dissipation range shows a slow energy decay with an approximate -3 scaling law. This slow decay starts at a normalized wavenumber around $\kappa_1\eta = 0.015$, which is associated with a spatial length scale of approximately 3 mm. Thus, it is found that the dissipation range exists for spatial scales of smallest lengths at 40–50 μm to the length scale of 3 mm, which is approximately 60 times the Kolmogorov scale. This is consistent with the definition by Pope (2000) where demarcation length scales are approximated at $\ell_{DI} = 60\eta$.

3.6. *Lower-Reynolds-number BMHV flows*

Simulations of lower peak Reynolds numbers are modelled to demonstrate BMHV flow fields of different physiologic conditions. A comparison of peak flows are shown

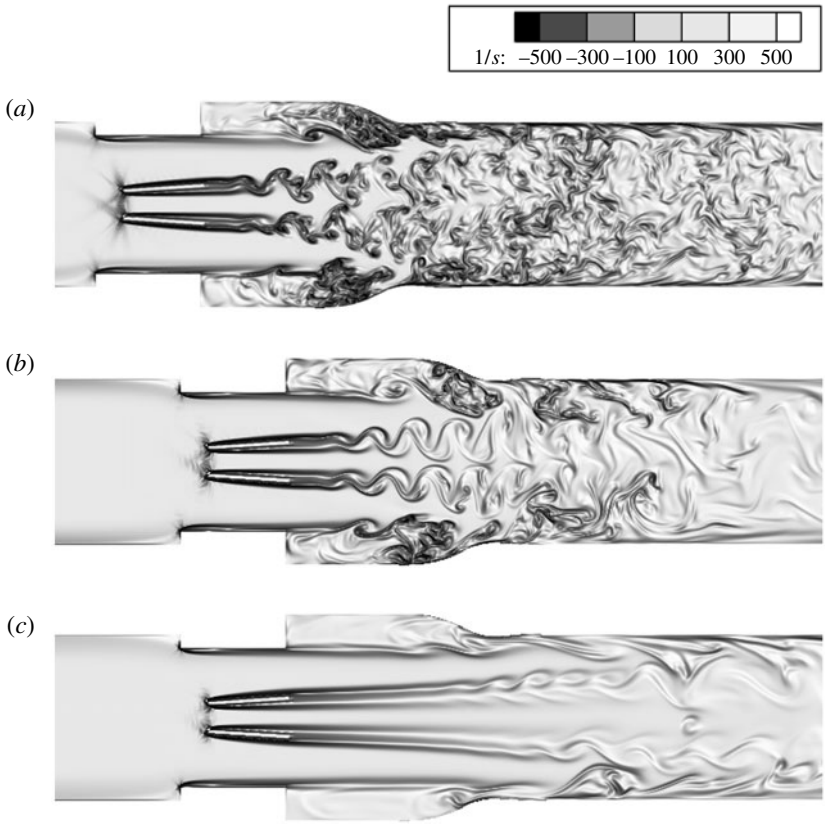

FIGURE 25. Comparison of peak-flows for simulations of different peak Reynolds numbers: (*a*) adult, peak $Re = 5780$; (*b*) child, peak $Re = 4418$; (*c*) infant, peak $Re = 2725$.

(figure 25) across simulations typical of adult, five-year-old child and six-month-old infant flows.

The vorticity plots show that adult peak flows ($Re = 5780$) are characterized by many small-scale eddies occupying the entire flow domain (figure 25*a*). At peak Reynolds number for the child flows ($Re = 4418$), vortex wakes are formed past the leaflet tips and recirculation regions in the sinus expansion are also observed (figure 25*b*). However, the leaflet vortex wakes are more coherent for the child case and do not break apart into smaller eddies. The sinus recirculation region is also weaker in comparison with adult flows.

In comparison with adult flows, peak flow for the infant case ($Re = 2725$) is shown to be very different (figure 25*c*). Flow past the leaflets are shown to form triple jet structures with no formation of vortex wakes as in child and adult flows. In addition, there is little to no recirculation within the sinus expansion region. Whereas adult peak flows show vortical structures throughout the entire flow domain, infant peak flows show triple orifice jets and few vortical structures.

Viscous shear stress fields are demonstrated at peak flow for each of the three flow cases (figure 26). This comparison shows the relatively moderate shear stresses in leaflet shedding vortices for the adult and child flows. Although flows are most unstable and disorganized in adult flows, the shear stress magnitudes of adult peak flow (figure 26*a*) are shown to be lowest of the three cases.

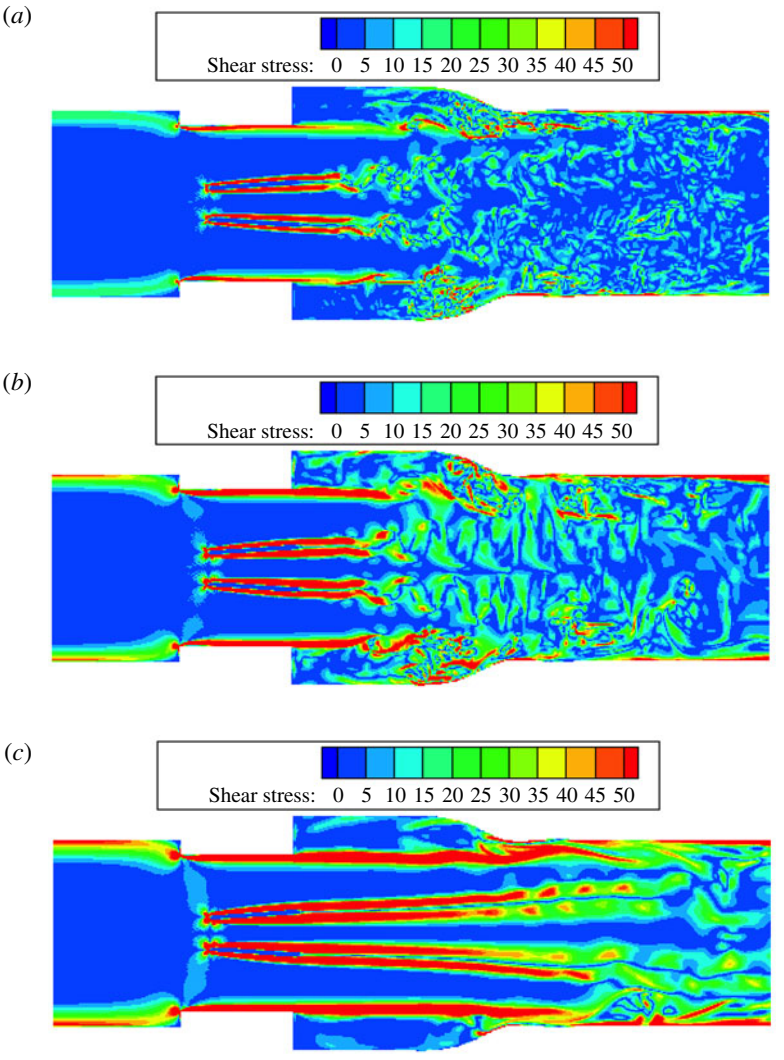

FIGURE 26. Comparison of viscous fluid shear stresses at peak flows for simulations of different peak Reynolds numbers: (*a*) adult, peak $Re = 5780$; (*b*) child, peak $Re = 4418$; (*c*) infant, peak $Re = 2725$.

The child flow shear stress field (figure 26*b*) is qualitatively similar to adult flow, but with higher shear stress magnitudes immediately downstream of the leaflet tips and sinus step expansion. The infant flow case (figure 26*c*) shows very high shear stresses in flow past the valve in thin shear layers. These thin shear layers are formed very close to solid surfaces of the valve, such as the leaflets and valve housing. The thin shear layers then extend into the sinus expansion and aortic chamber while gradually expanding in width. These shear layers are associated with very high shear stress magnitudes, but not with recirculation or mixing of flow. As the shear layers expand in width in the aortic chamber, shear stress magnitudes are lowered and a wider region of flow is encompassed.

Mean flow and root-mean-square (r.m.s.) velocity profiles across the three cases are compared at peak flow for each case. Velocity profiles are compared (figure 27)

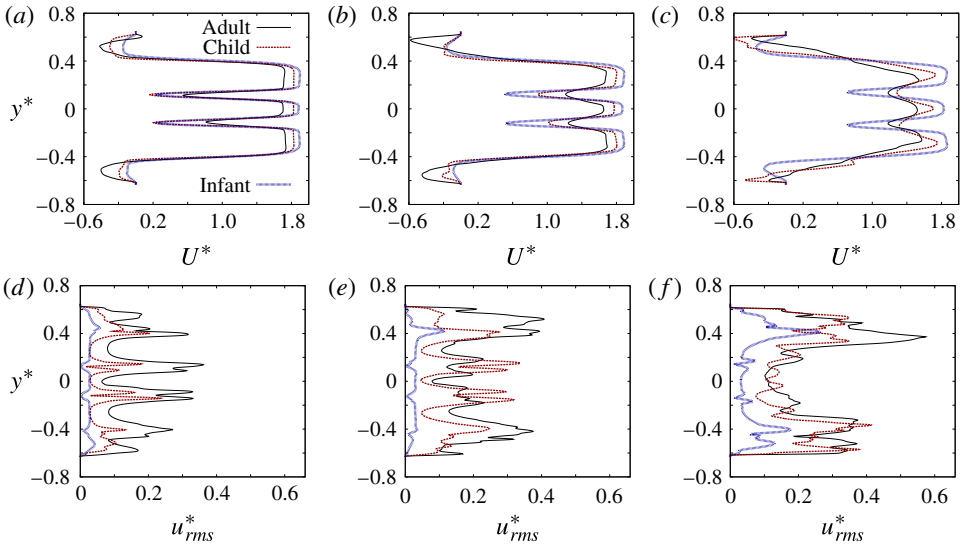

FIGURE 27. (Colour online) Mean flow and r.m.s. velocity profile comparison at peak flow for BMHV flows of adult, child, and infant cases: (*a*) $x^* = 0.2$; (*b*) $x^* = 0.4$; (*c*) $x^* = 0.8$; (*d*) $x^* = 0.2$; (*e*) $x^* = 0.4$; (*f*) $x^* = 0.8$.

using normalized mean velocities U^* and normalized r.m.s. velocities u^*_{rms}, where the averaged velocities are normalized by average inlet velocity at peak flow for each case. The normalized axial position of comparison x^* and normalized perpendicular position y^* are normalized by characteristic length L, which is taken as the inlet diameter for each case.

Mean flow comparison (figure 27*a–c*) show similar profiles for all three flow cases in the form of triple orifice jets. It is observed that as peak Reynolds number decreases, the normalized peak velocities for the triple orifice jets increase. Further downstream of the valve (figure 27*c*), the adult and child flow profiles become less organized compared with infant flow. These observations are explained by the more laminar and coherent forward flow nature of the lower-Reynolds-number infant flow. Although the mean flow profiles change further downstream of the valve for the adult flow case, the flow profiles for infant flow remain very similar across all comparison points. It is also seen that the paediatric flows have lower reverse velocity regions near the edges of the domain. This quantitatively demonstrates the lower recirculation regions in the sinus expansion and again shows the more coherent forward flow nature for the lower-Reynolds-number paediatric flows.

Root-mean-square velocity profiles show clear differences between the higher-Reynolds-number adult flows and the paediatric flows. For all three cases, r.m.s. velocities increase further downstream of the valve, demonstrating higher fluctuations in the flow fields as vortices are shed from the leaflets and valve housing and spread through the domain. At the comparison point at the edge of the sinus expansion (figure 27*f*), adult and child flows show relatively similar r.m.s. velocity magnitudes. However, for all lines of comparison, the infant flows show consistently lower normalized r.m.s. values. This quantitatively demonstrates the more coherent and laminar flows for paediatric-sized valves, and particularly infant flows.

Energy spectra are created at peak flow for the paediatric cases to determine quantitative differences in turbulence across all three cases (figure 28). As with

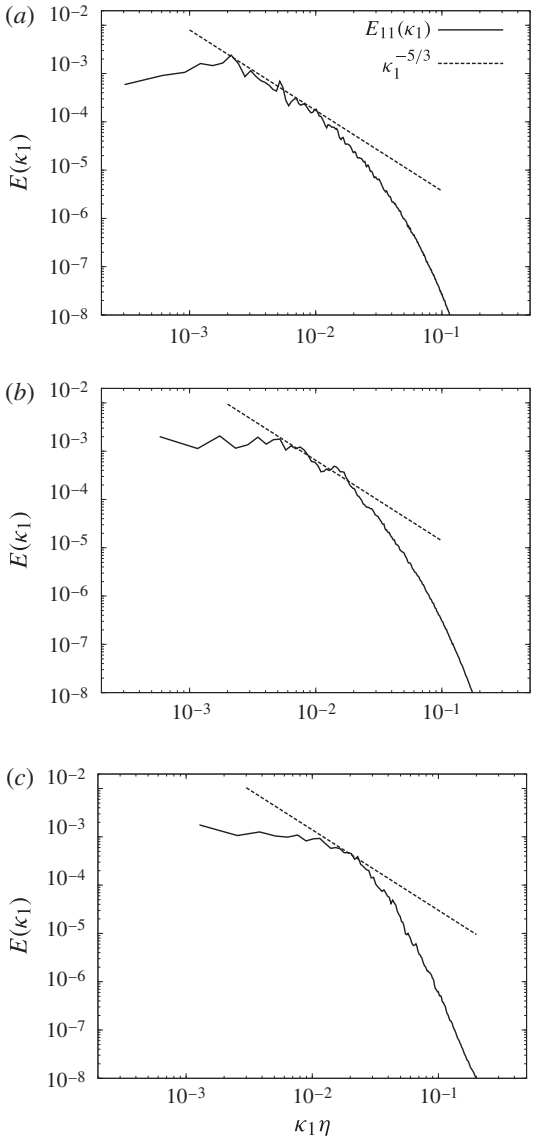

FIGURE 28. Comparison of 1D energy spectra at peak flow for BMHV flows of (*a*) adult, (*b*) child and (*c*) infant cases.

the adult case, the energy spectra are plotted for the streamwise axial direction as most appropriate for generating spectra. The wavenumber x-axis is normalized by an approximated Kolmogorov scale η. This is estimated at 50 μm for adult flow, and scaled for child and infant flows as 61 and 88 μm, respectively.

For adult flows, the inertial range shows a good fit with the $-5/3$ law for a range of wavenumbers ($\kappa_1\eta = 0.004$–0.015) that demonstrates the presence of turbulence at peak flow. For child flow, the $-5/3$ fit is not as good in any part of the inertial range, and shows slight matching in the inertial range for only a small range of wavenumber modes ($\kappa_1\eta = 0.007$–0.01). Although not as good as in the adult flow case, this

demonstrates that even at lower-Reynolds-number child flows, some turbulence may exist at peak flows.

Energy spectra at peak flow for the infant case shows no clear matching with the $-5/3$ line, and no clear demonstration of turbulence for this lowest-Reynolds-number case. It is clearly shown from these energy spectra that there is a quantifiable difference for the presence of turbulence for BMHV flow at different physiologic conditions. The energy spectra along with the comparison of r.m.s. values (figure 27*d–f*) reinforces the qualitative observations of more coherent, laminar peak flows for the paediatric cases, particularly for the infant flows.

4. Discussion

The numerical simulations detail complex flow features that could not be captured by particle image velocimetry (PIV) experiments. During leaflet opening (figure 4), an interesting feature of a b-datum reverse jet is observed. This seems to form owing to the leaflets rapidly opening and pushing back quasi-static flow on the ventricular side. Although this jet flows immediately towards the ventricular side from leaflet opening, the forward flow pushes this fluid towards the aortic side at the onset of systole.

Because the leaflet motion and flowrate are prescribed from experimental data, this b-datum reverse jet may be owing to a slight synchronization offset in the numerical simulations. The LBM is an explicit time-marching method and thus the forward flow may not reach the valve when the leaflets are prescribed to open, leading to the quasi-static flow on the ventricular side. Although there is a slight synchronization offset, the high temporal resolution of the simulations (2.4 μs) as compared with the leaflet opening time ($\sim$60 ms) make the offset issues very minor. However, in the special case of leaflet opening, the prescribed leaflet motion dictates that the leaflets suddenly open at the beginning of systole, when the flowrate is near zero. In this special case, the prescribed leaflet motion and synchronization offset lead to flow near the b-datum jet being pushed towards the ventricular side. Although the dual opening leaflet wakes do occur in experimental observations, the reverse b-datum jet in leaflet opening is attributed as a special artifact of the numerical simulations.

In peak flow (figure 6), coherent vortical structures that shed from the leaflet tips quickly break down into smaller eddies. These small-scale vortices are captured at the higher 80 μm resolution simulations but appear as a disorganized mix in coarser resolution simulations (not shown) and other numerical studies, thus highlighting the ability of this numerical method and importance of higher spatial resolution simulations to capture smaller vortical scales.

Starting at accelerating flow (figure 9), interaction occurs between flow past the leaflet tips and the recirculation region caused by the sinus expansion. Native aortic sinuses have a more gradual expansion compared with the sudden step expansion of this study. However, recirculation regions are known to exist in native aortic valve flows owing to the sinus expansion root. This simulation highlights the potential mixing of vortex shedding flows past the leaflet tips with sinus recirculation zones.

Figures 10 and 11 show peak or near-peak flow with the coherent vortices shed from the leaflet tips quickly breaking into smaller eddies. It is noted that these smaller structures form downstream of the valve, sometimes at the downstream edge of the sinus expansion. Thus, the uniform high spatial resolution of this method captures these small eddies throughout the domain without concentrating high resolution to the valve, as in other studies (Dasi *et al.* 2007; De Tullio *et al.* 2010). The breakup of large coherent vortices into smaller structures at higher-Reynolds-number causes the

spreading of the vortex street throughout the flow domain. In the sinus expansion, the recirculation region is also shown to grow in size and vorticity magnitude. This combination leads to increased mixing of the two flow regimes (leaflet tip vortices and sinus expansion recirculation) at peak flow as seen in figure 11.

A natural sinus region is more gradual in its expansion, and the shape of the sinus in the simulations has been idealized to a sudden axisymmetric expansion. This is taken directly from a microCT scan of the experimental flow set-up. The sudden expansion may lead to stronger sinus flow recirculation, due to vortex shedding caused by flow past the sharper step expansion. The idealized sinus geometry primarily induces stronger flow recirculation in the sinus expansion and does not affect the formation of leaflet vortex wakes. However, further downstream of the valve, the strong sinus recirculation region mixes with the vortex wakes past the leaflet. This flow mixing may be more prominent due to the idealization of the sinus geometry. However, this flow mixing occurs downstream of the valve and sinus regions and is likely to occur even in the presence of a more natural sinus geometry.

During the closing phase (figure 7), the leaflets slam shut and result in three strong closing leakage jets. It is possible that blood elements such as platelets could experience high shear stresses if trapped in these leakage jets, and may possibly contact the leaflets as well. The closing leakage jets, although strong, dissipate quickly in the flow on the ventricular side. It should be noted that the b-datum leakage jet upon closing is directed centrally upstream, owing to the imposed symmetric closing of the leaflets.

Leaflet closing is characterized by quick washout of vortical structures downstream of the valve owing to the low overall flowrate (figures 13 and 14). High instantaneous shear stress regions are observed near the leaflet tips, however, where there is rapid motion of the solid leaflet surface. When the leaflets contact the valve housing figure 15, symmetrical structures are observed owing to the symmetric prescribed closing of the leaflets. A small initial leakage jet is actually directed downstream towards the aortic side (figure 15*a*) owing to the rapid reduction in orifice area in the central b-datum plane. Immediately afterwards, three coherent leakage jets form simultaneously from leaflet contact with the housing and a b-datum jet in the ventricular direction. These features are symmetric upon initial formation, but as the leakage jets spread outwards they become more disorganized, growing in size but weakened in strength (figure 15*d*). The closing of the leaflets also causes an unstable mix of structures on the immediate aortic side of the leaflets. Figure 29 shows the viscous shear stress plot at leaflet impact for the flow domain at a 2D slice, which demonstrates a very high instantaneous shear stress at the b-datum jet but rapid decrease in shear stress values throughout the rest of the domain.

In diastolic flow (figure 8), a strong b-datum leakage jet is shown in this time snapshot with leakage flow drifting towards the top side. This snapshot is taken in mid diastolic flow, although the b-datum leakage jet does oscillate in direction. This oscillation is highlighted by the varying direction of leakage flows shown in figure 19(*a*,*b*). However, even with the oscillating direction of the central jet, it is observed that the jet prefers one wall over the other during diastole. This asymmetry of the b-datum leakage jet is observed even under idealized computational conditions where the domain geometry, leaflet motion and inlet flow profile are all symmetric. As we eliminate design or flow condition asymmetries in our computational model, this observed leakage jet asymmetry is likely owing to the disorganized nature of pulsatile high-Reynolds-number BMHV flow.

The authors believe that the asymmetry is likely owing to interaction with larger-scale vortices on the ventricular side that come into contact with the incoming

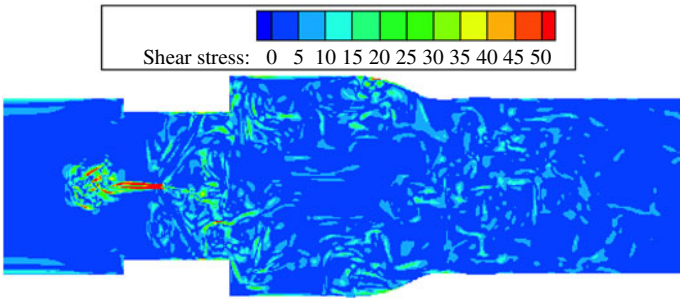

FIGURE 29. Shear stress (dynes cm^{-2}) plot at leaflet impact with housing.

b-datum leakage jet. Mixing can occur between the leakage jet from the b-datum plane with strong vortical structures on the bottom half of the ventricular side, as shown in figure 19(*b*). The flow on the ventricular side is highly disorganized and in turn the large-scale vortices are not symmetric about the b-datum plane. This unorganized and asymmetric vorticity field is again highlighted in figure 19(*c*,*d*). In both of these figures, the leakage jet shows a slight drift towards the side with the stronger (black and white contours) vortical structures even before their direct interaction. Thus, it is postulated that the asymmetry in the large-scale vortices would interact with the b-datum leakage jet and cause an oscillation in direction. However, it can also be expected that asymmetry of the large-scale vortices would lead to a preferential direction for the b-datum jet over time. It is primarily observed that the section of the ventricular side with stronger vortical structures tends to 'pull' the b-datum leakage jet into interaction.

Leaflet–valve leakage jets may interact with the incoming b-datum jet to also influence its direction. Upon leaflet impact, a centrally flowing b-datum jet is observed with two large vortical structures emanating from the valve walls towards the b-datum jet (figure 30*a*). Then 20 ms later, these two large vortices begin to interact with the b-datum jet, causing a wave-like formation in the central jet (figure 30*b*). After an additional 8 ms, the b-datum jet is shown to be oscillating in direction owing to further interaction with the leaflet–valve vortices (figure 30*c*). These snapshots, taken milliseconds apart, show how even in a simulation with perfect symmetrical design, the disorganized nature of pulsatile flow in BMHVs causes the b-datum jet to oscillate in direction owing to interaction with various vortical structures.

This asymmetric drifting motion of the diastolic leakage jet occurs in the mid-diastole phase as well. Upon leaflet closing, the central b-datum jet is shown to spread outwards towards the ventricular side in figure 31(*a*). However, it is noted that as the central jet widens, vortical structures are slightly asymmetric with slight bias towards the top side. A timepoint 40 ms later (figure 31*b*) shows that this initial leakage jet has weakened, but has also spread wider throughout the ventricular side. After an additional 80 ms (figure 31*c*), a secondary b-datum leakage jet begins to form through the central orifice. However, it is noted that the previous leakage jet structure has spread throughout the ventricular side with dispersed, but weaker vortical structures. These vortices are not symmetric, but rather show a bias towards the top side. The secondary b-datum leakage jet shows slight asymmetry at this timepoint favouring the top side, with a slight pull from the larger vortical structures but without direct interaction. After an additional 80 ms (figure 31*d*), the b-datum leakage jet is shown to interact with the larger vortices, pulling upwards towards the

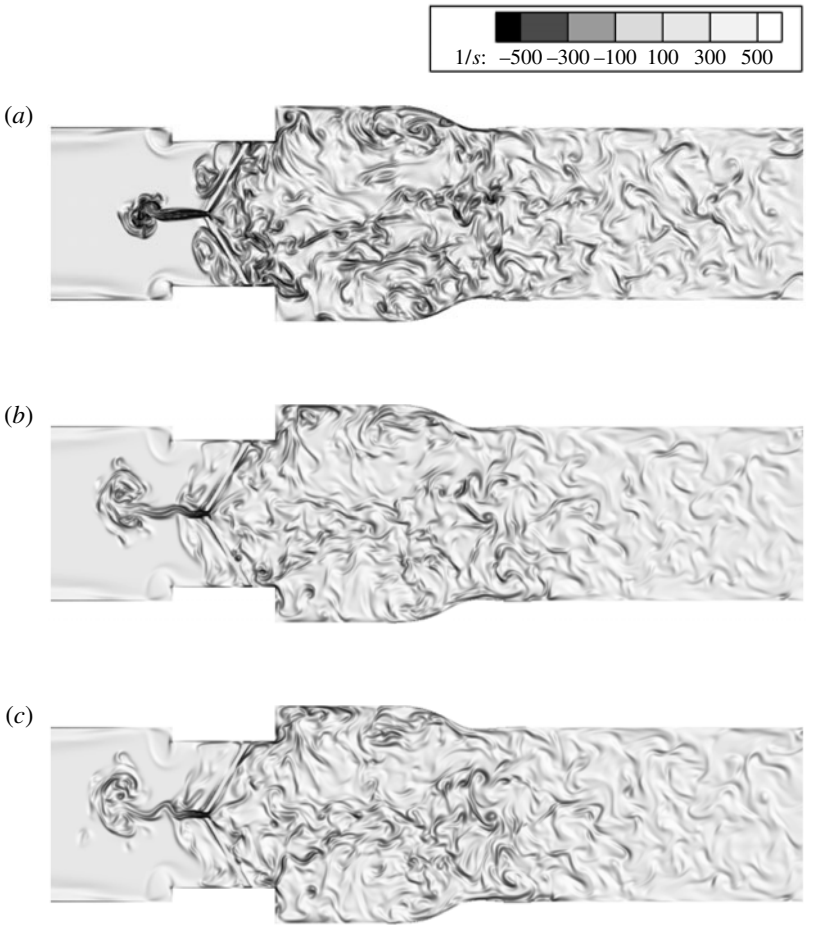

FIGURE 30. Interaction of b-datum jet with leaflet–valve jets causing asymmetry in jet direction. Vorticity magnitude scaling identical for all plots. (*a*) Triple leakage jets with initial formation and growth. (*b*) Initial interaction between leaflet–valve jets with b-datum jet. (*c*) Development of asymmetry in b-datum jet owing to leakage jet interaction.

top side where the large-scale vortices are located. This demonstrates that even under idealized conditions, the initial leakage jet spreads asymmetrically and influences the pull direction of the mid-diastolic secondary b-datum leakage jet.

It is observed in coarser 160 μm simulations that for multiple cardiac cycles, the mid-diastolic leakage jet always oscillates in time and prefers one wall direction, although the degree of asymmetry and frequency of oscillation in the leakage jet varies from cycle-to-cycle. This further highlights the highly disorganized nature of pulsatile flow through BMHVs even in the low flowrate diastolic phase. This could also have implications of platelet damage incurred in the b-datum leakage jet. The oscillations and preferential jet direction would lead to platelets not advecting centrally towards the ventricular side where the vortical structures dissipate, but rather being caught in the large-scale vortices, thus increasing their exposure time to higher surface shear stresses. This would increase the chances of thromboembolic complications incurred in diastolic flows, beyond those complications already known

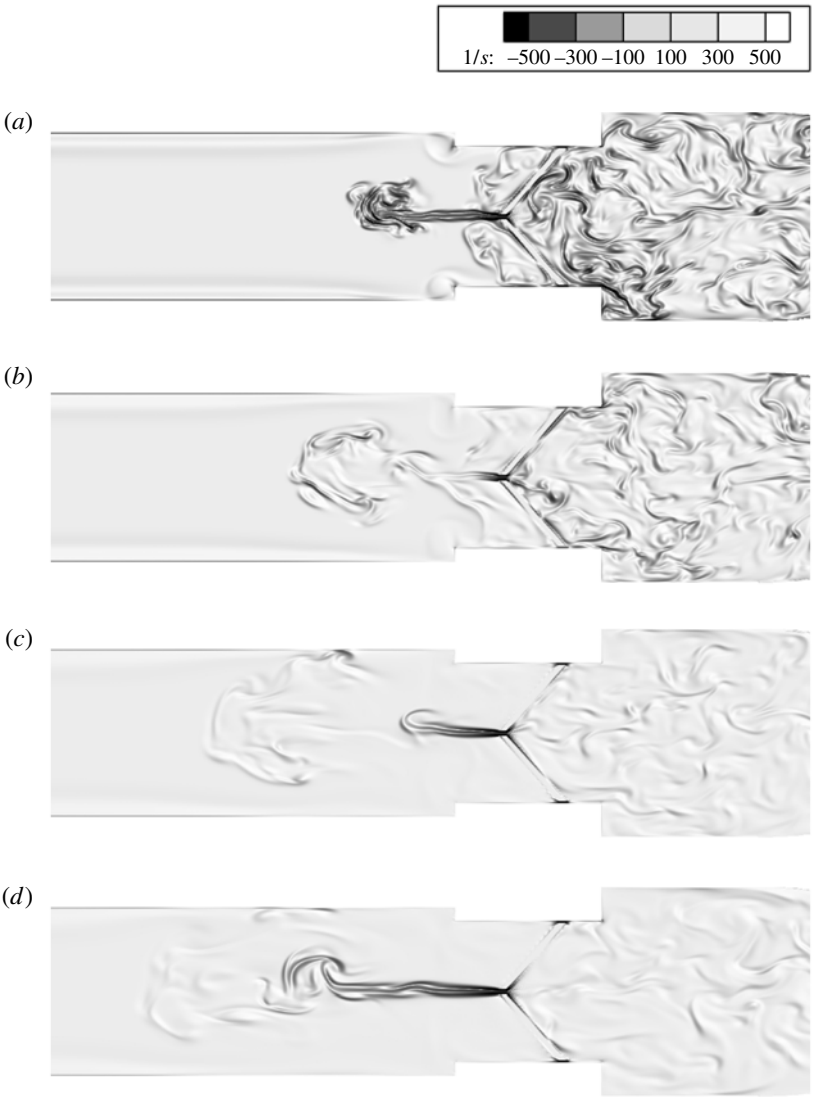

FIGURE 31. Asymmetric drift of central b-datum jet in diastolic phase. Vorticity magnitude scaling identical for all plots. (*a*) Initial jet flowing centrally upon leaflet closure. (*b*) Dissipation of first central b-datum jet. (*c*) Secondary jet forming through b-datum gap. (*d*) Slight asymmetric pull towards remnants of first jet.

to occur in the hinge regions. Using the platelet damage quantification method with LBM–external boundary force (EBF) (Wu *et al.* 2011; Yun *et al.* 2012), these high-risk regions can be further analysed in future simulations.

It has been noted in previous studies (Dasi *et al.* 2007) that there is a natural asymmetry in leaflet motion from cycle to cycle. The simulations of this study prescribe idealized symmetric leaflet motion to best represent an averaged cardiac cycle of BMHV flow. Even under these idealized conditions, asymmetric leakage jets are observed in the diastolic phase. The natural variation of leaflet motion would exacerbate these asymmetries, as the leaflets would impact the valve housing at

different times. Consequently, leakage jet mixing would be more asymmetric due to the difference in timing of leaflet–valve impacts. The exposure time of platelets to these asymmetric large vortices would be increased and thus there may be higher potential for blood elements to be damaged. This may be explored in future studies.

To the best of the authors' knowledge, this study is the first quantification of turbulent energy mean dissipation rates, ϵ, and generation of energy spectra for computational simulations of BMHV flow. The results of this analysis have shown the Kolmogorov scales to be of the order of 40–60 μm. These small scales are shown to exist downstream of the valve, highlighting the need for high spatiotemporal resolution simulations throughout a large portion of the flow domain to capture intricate flow features.

The calculation of mean dissipation rates demonstrates that the local isotropy approximation ϵ_{iso} is a good approximation for BMHV flows, with high goodness-of-fit R^2 values throughout the flow domain. This has implications for future experimental studies that are limited to the local isotropy approximation, as mean dissipation rates and Kolmogorov scales can be closely estimated with 2D plane data. The calculation of dissipation rates can also be used to determine the location of small scale eddies in this flow. The high fluctuations associated with these small eddies may be linked to an increased potential for blood damage in these flow regions.

Although dissipation rates confirm that small features of BMHV flow are located in the leaflet wakes and sinus recirculation regions, they do not capture how the turbulent energy is distributed in various length scales. This study is the first quantification of turbulence for numerical simulations with a delineation of inertial and dissipative spatial scales for BMHV flow. The energy spectra demonstrates the development of an inertial range, but only for a small range of wavenumber modes and thus not a clear demonstration of turbulence. The inertial range is approximated for length scales of the order of 3–12 mm, which encompasses less than a decade of wavenumbers ($\kappa_1\eta = 0.004$–0.015). It should be noted that the highest scale of this inertial range of 12 mm is close to the pipe radius of 12.7 mm. It is also interesting to note that the length scale where the spectra breaks off from the $-5/3$rd slope is roughly 3 mm, which is approximately 60 times the Kolmogorov scale. This is remarkably consistent with the demarcation length scale defined as $\ell_{DI} = 60\eta$ in Pope (2000) as a convenient measure that separates the inertial and dissipative scales.

Turbulence has implications for aortic valve flows, particularly for flows through prosthetic valves. The presence of a mechanical valve may lead to the onset of turbulence, although energy spectra have not been performed for native valve flows and thus a direct comparison cannot be performed. Turbulent flows are generally characterized by unsteady shear stresses and increased mixing, and have been previously associated in literature with increased blood damage. A comparison with turbulence in native valve flows may help provide a link between turbulence and blood damage complications associated with prosthetic valves.

Blood damage is thought to occur owing to shear stresses and exposure time on suspended elements. In the case of aortic valve flows where the small-scale eddies are an order of magnitude larger (40–50 μm) than the blood elements (3–8 μm), suspended elements may experience viscous shear stresses primarily due to relative motion of the fluid. This may cause complications such as haemolysis, platelet activation, and thrombosis, and thus the viscous fluid shear stresses are of primary interest. The unsteady fluid velocities that are present in turbulent flows may be tied to both increased and unsteady shear stresses on suspended red blood cells and platelets. As proposed by Antiga & Steinman (2009), the velocity fluctuations

present in turbulence may also lead to energy dissipation in cell–cell interactions, thus increasing viscous stresses and blood damage experienced by suspended elements. In addition, the increased mixing caused by turbulent flows can lead to recirculation paths for suspended elements, thus increasing their exposure time to unsteady and high shear stresses.

This combination of unsteady and increased shear stresses and higher mixing in turbulent flows can be tied to the thromboembolic complications that are clinically observed to form in BMHV flows. The link between blood damage and turbulence could be clarified by DNS simulations with spatial resolution of the order of suspended blood elements and with dense suspension modelling. However, current computational resources prohibit such simulations on as large a scale as BMHV flows. A smaller scale and simplified study with dense suspension flow at varying Reynolds numbers could provide this link between turbulence and blood damage with reasonable computational expenses.

The unsteady shear stresses and mixing of turbulent flows may lead to other physiological complications for aortic valve flows, such as calcification of native leaflets. Although the mechanical leaflets of this study are thromboresistant, future studies examining biological leaflets in other artificial valve flows (such as bio-prosthetic valves) may quantify turbulence to link the presence of turbulence with leaflet calcification complications. The presence of turbulence in aortic flows can also be linked to irreversible pressure loss in prosthetic valve flows (Dyverfeldt *et al.* 2013) owing to kinetic energy dissipation. This irreversible pressure loss leads to the left ventricle responding with increased work, which leads to increased stress on the myocardium.

The link between turbulence and various complications of BMHV flow are yet unclear. This study demonstrates the presence of turbulence in BMHV flows but cannot directly associate this with blood damage complications, as this is outside the scope of this study. If such a connection between turbulence and prosthetic device complications is made in future studies, prosthetic device development can be aimed to avoid turbulent flows in order to prevent serious complications.

The comparison of the physiological adult case and paediatric cases show strong differences in flow features and fluid shear stresses. The adult peak flow shows many small-scale vortices throughout the domain as compared with the paediatric cases (figure 25). Although the flow features of the lower-Reynolds-number cases are more coherent and stable, they demonstrate higher fluid shear stresses throughout the flow fields (figure 26).

Although peak Reynolds number for these example paediatric flows are lower, bulk average velocities are higher. Reynolds number can be written in terms of flowrate as

$$Re = \frac{U_{avg} D}{\nu} = \frac{4Q}{\pi D \nu} \tag{4.1}$$

where Q is inlet flowrate. Flowrate and leaflet motion variation curves for the paediatric cases can be found in literature (Yun 2014; Yun *et al.* 2014*b*). In these example simulations, the cardiac output (directly related to inlet flowrate Q) scales down by a smaller factor than valve sizing scales down. This results in lower peak Reynolds numbers for the paediatric cases, which explains the more coherent and stable flows. However, average inlet velocity ratio across simulation cases can be expressed as

$$\frac{U_2}{U_1} = \frac{Q_2}{Q_1} \cdot \frac{D_1^2}{D_2^2}. \tag{4.2}$$

Although Reynolds numbers and cardiac outputs decrease in these examples, the relative valve size scaling results in higher flow velocities. In addition, the more laminar nature of the lower-Reynolds-number flows may result in higher velocity gradients for flow past the valve. These higher velocity gradients extend to the more coherent flows past the valve and into the sinus. As velocity gradient is directly related to viscous shear stresses, this also means that viscous shear stresses are higher in more laminar flow past the valve. This is observed in the infant flow case, where high shear stress magnitudes are observed close to the leaflet and valve housing surfaces as well as in the jets downstream of the valve, in the form of thin shear layers. The aortic sinus is characterized by high shear stresses in thin shear layers downstream of the leaflet and valve housing surfaces, but lower shear stress values in the middle of each orifice flow and within the sinus expansion. This is in contrast to the adult and child flow cases, where shear stress magnitudes are lower but the entire sinus region is filled with moderate levels of shear stress from the more disorganized and mixing flow fields.

Quantitative comparison of the three BMHV flow cases are made as well (figure 27). The mean flow plots show that infant flow profiles remain very similar even far downstream of the valve. This is due to the triple orifice jet structure of infant flow that do not break apart but remain coherent. The higher-Reynolds-number adult and child flows show variation in the flow profiles further downstream of the valve (figure 27*c*), likely due to the breakdown of shed vortices into small-scale structures both for the leaflet wakes and the sinus recirculation region, which is most pronounced in adult flows. This confirms the qualitative observation of more disorganized and unstable flow for the higher-Reynolds-number adult flows. The adult case also shows strong reverse flow velocities near the domain surfaces for mean flow plots, quantitatively demonstrating the high recirculation regions in the sinus expansion. The r.m.s. velocity plot for adult flow (figure 27*f*) also demonstrates highest values further downstream of the valve, where the most small-scale eddies are observed for the leaflet wakes and recirculation zones, and where high-flow mixing occurs. Across all r.m.s. velocity comparisons (figure 27*d–f*), lowest-Reynolds-number infant flows consistently show lower fluctuating velocities than adult flows. This quantitatively demonstrates the more coherent and laminar nature of lower-Reynolds-number infant BMHV flows.

The comparison of energy spectra (figure 28) clearly demonstrates the difference in the presence of turbulence across all three cases. Whereas the higher-Reynolds-number adult flow shows a clearer demonstration of an inertial range that fits the Kolmogorov $-5/3$ scaling law, the child case shows an unclear fit over a smaller range of wavenumber modes. More significantly, the lowest-Reynolds-number infant case shows no demonstration of an inertial range, again confirming that this example infant flow is more coherent and laminar in nature.

The comparative blood damage potential for the paediatric examples is yet unclear from these simulations. Although the paediatric flow examples show more coherent flows, it is noted that the viscous shear stress magnitudes are higher in these example flows than for the adult case. Although the shear stress magnitudes are higher for lower-Reynolds-number paediatric flows, the more coherent flows would mean blood elements suspended in these flows are not subjected to highly unsteady shear stresses as in adult BMHV flows. It is still unclear what effect dynamic stress loading has on blood element damage, although it is believed to increase blood damage potential. In addition, the more coherent paediatric flows may lead to less flow mixing and recirculation zones, which are also thought to lead to blood element damage. Thus,

the higher viscous stresses in the paediatric flow fields of these simulations may not necessarily lead to higher blood damage potential due to less flow mixing and recirculation, and less dynamic shear stress loading.

The simulations of paediatric BMHV flows are performed as comparison points of alternative physiologic conditions. These are simulations of typical values for child and infant flows, however the results do not necessarily extend to all paediatric flows. Future simulations may employ a wider range of paediatric flow conditions to observe the variation in flow fields with more comparison to physiologic adult BMHV flows. Future simulations may also employ the use of suspended particles to track and quantify damage to blood elements in these various BMHV flows. Further understanding the nature of how blood damage occurs will help to clarify these results and the potential for blood damage in lower-Reynolds-number paediatric BMHV flows.

5. Conclusion

The LBM has been used in this study to simulate full-BMHV pulsatile flows with leaflet motion and two-way flow at the highest spatiotemporal resolution to date. Simulations at this resolution are able to capture fine-scale features at high-Reynolds-number. At peak flow, coherent vortices shed past the leaflet tips break down into smaller-scale eddies that are not captured in previous studies. These eddies are also seen to interact with the sinus expansion recirculation zone. The simulations have also highlighted leaflet closing and diastolic flow features with unseen detail, in particular capturing asymmetric and oscillating b-datum leakage jets during mid-diastole and quantifying axial velocities and fluid shear stress variation throughout the diastolic phase. The authors have also quantified turbulence in this BMHV flow for the first time with numerical simulations, showing turbulent dissipation rates and energy spectra at peak flow with inertial range development. Lower-Reynolds-number BMHV flows were also simulated modelling paediatric flows, and showed more coherent and laminar flows both qualitatively and quantitatively. Although shear stress magnitudes were found higher in the paediatric flows, it is unclear how paediatric flows may differ from adult flows in terms of blood damage potential. Energy spectra analysis of the flows showed that while adult flows demonstrated an inertial range indicative of turbulence, child flows showed a shorter and less clear inertial range, and infant flows showed a lack of any inertial range.

The authors have demonstrated in previous studies that LBM in combination with the EBF method is able to accurately quantify platelet damage in BMHV flows on a smaller scale in the hinges when compared with blood damage experiments (Wu *et al.* 2011; Yun *et al.* 2012). The LBM–EBF method can now be included to accurately quantify platelet damage in pulsatile flows throughout the entire BMHV geometry in future studies across varying physiologic conditions.

Acknowledgements

This research was carried out under a grant from the National Heart, Lung and Blood Institute (HL-07262). Computational simulations were performed using resources from XSEDE: extreme Science and Engineering Digital Environment (TG-CTS100012). The authors would also like to thank N. Saikrishnan and K. Iyer for their useful comments in the development of this work. We appreciate discussion and input from Dr P. K. Yeung.

REFERENCES

AIDUN, C. K. & CLAUSEN, J. R. 2010 Lattice Boltzmann method for complex flows. *Annu. Rev. Fluid Mech.* **42**, 439–472.

AIDUN, C. K. & LU, Y. 1995 Lattice Boltzmann simulation of solid particles suspended in fluid. *J. Stat. Phys.* **81** (1), 49–61.

AIDUN, C. K., LU, Y. & DING, E. J. 1998 Direct analysis of particulate suspensions with inertia using the discrete Boltzmann equation. *J. Fluid Mech.* **373**, 287–311.

ANTIGA, L. & STEINMAN, D. A. 2009 Rethinking turbulence in blood. *Biorheology* **46** (2), 77–81.

BLACK, M. M. & DRURY, P. J. 1994 Mechanical and other problems of artificial valves. *Pathol. Devices* **86**, 127–159.

BORAZJANI, I., GE, L. & SOTIROPOULOS, F. 2008 Curvilinear immersed boundary method for simulating fluid structure interaction with complex 3D rigid bodies. *J. Comput. Phys.* **227** (16), 7587–7620.

BORAZJANI, I. & SOTIROPOULOS, F. 2010 The effect of implantation orientation of a bileaflet mechanical heart valve on kinematics and hemodynamics in an anatomic aorta. *Trans. ASME J. Biomech. Engng* **132**, 111005.

BROWN, M. L., PARSHEH, M. & AIDUN, C. K. 2006 Turbulent flow in a converging channel: effect of contraction and return to isotropy. *J. Fluid Mech.* **560**, 437–448.

DASI, L. P., GE, L., SIMON, H. A., SOTIROPOULOS, F. & YOGANATHAN, A. P. 2007 Vorticity dynamics of a bileaflet mechanical heart valve in an axisymmetric aorta. *Phys. Fluids* **19**, 067105.

DASI, L. P., MURPHY, D. W., GLEZER, A. & YOGANATHAN, A. P. 2008 Passive flow control of bileaflet mechanical heart valve leakage flow. *J. Biomech.* **41** (6), 1166–1173.

DE TULLIO, M. D., CRISTALLO, A., BALARAS, E. & VERZICCO, R. 2010 Direct numerical simulation of the pulsatile flow through an aortic bileaflet mechanical heart valve. *J. Fluid Mech.* **622**, 259–290.

DING, E. J. & AIDUN, C. K. 2003 Extension of the lattice-Boltzmann method for direct simulation of suspended particles near contact. *J. Stat. Phys.* **112** (3), 685–708.

DUMONT, K., VIERENDEELS, J., KAMINSKY, R., VAN NOOTEN, G., VERDONCK, P. & BLUESTEIN, D. 2007 Comparison of the hemodynamic and thrombogenic performance of two bileaflet mechanical heart valves using a CFD/FSI model. *Trans. ASME J. Biomech. Engng* **129**, 558–565.

DYVERFELDT, P., HOPE, M. D., TSENG, E. E. & SALONER, D. 2013 Magnetic resonance measurement of turbulent kinetic energy for the estimation of irreversible pressure loss in aortic stenosis. *JACC: Cardiovasc. Imag.* **6** (1), 64–71.

ELLIS, J. T., HEALY, T. M., FONTAINE, A. A., SAXENA, R. & YOGANATHAN, A. P. 1996 Velocity measurements and flow patterns within the hinge region of a Medtronic Parallel bileaflet mechanical valve with clear housing. *J. Heart Valve Disease* **5** (6), 591–599.

FALLON, A. M., SHAH, N., MARZEC, U. M., WARNOCK, J. N., YOGANATHAN, A. P. & HANSON, S. R. 2006 Flow and thrombosis at orifices simulating mechanical heart valve leakage regions. *Trans. ASME J. Biomech. Engng* **128**, 30–39.

GE, L., DASI, L. P., SOTIROPOULOS, F. & YOGANATHAN, A. P. 2008 Characterization of hemodynamic forces induced by mechanical heart valves: Reynolds vs. viscous stresses. *Ann. Biomed. Engng* **36** (2), 276–297.

GIERSIEPEN, M., WURZINGER, L. J., OPITZ, R. & REUL, H. 1990 Estimation of shear stress-related blood damage in heart valve prostheses – *in vitro* comparison of 25 aortic valves. *Intl J. Artif. Organs* **13** (5), 300–306.

GRIGIONI, M., CAPRARI, P., TARZIA, A. & D'AVENIO, G. 2005 Prosthetic heart valves' mechanical loading of red blood cells in patients with hereditary membrane defects. *J. Biomech.* **38** (8), 1557–1565.

HUNT, J. C. R., WRAY, A. A. & MOIN, P. 1988 Eddies, streams, and convergence zones in turbulent flows. In *Studying Turbulence Using Numerical Simulation Databases, 2. Proceedings of the 1988 Summer Program*, Report CTR-S88, vol. 1, pp. 193–208. Center For Turbulence Research.

JEONG, J. & HUSSAIN, F. 1995 On the identification of a vortex. *J. Fluid Mech.* **285**, 69–94.

KALDARAROVA, M., BALAZOVA, E., TITTEL, P., STANKOVICOVA, I., BRUCKNEROVA, I. & MASURA, J. 2007 Echocardiographic measurements of the aorta in normal children and young adults. *Bratisl. Lek. Listy* **108** (10–11), 437–441.

KAMENEVA, M. V., BURGREEN, G. W., KONO, K., REPKO, B., ANTAKI, J. F. & UMEZU, M. 2004 Effects of turbulent stresses upon mechanical hemolysis: experimental and computational analysis. *ASAIO J.* **50** (5), 418–423.

KEATING, B., VAHALA, G., YEPEZ, J., SOE, M. & VAHALA, L. 2007 Entropic lattice Boltzmann representations required to recover Navier–Stokes flows. *Phys. Rev.* E **75** (3), pp. 036712-1 to 036712-11.

KIM, J., MOIN, P. & MOSER, R. 1987 Turbulence statistics in fully developed channel flow at low Reynolds number. *J. Fluid Mech.* **177** (1), 133–166.

KRISHNAN, S., UDAYKUMAR, H. S., MARSHALL, J. S. & CHANDRAN, K. B. 2006 Two-dimensional dynamic simulation of platelet activation during mechanical heart valve closure. *Ann. Biomed. Engng* **34** (10), 1519–1534.

LADD, A. J. C. 1994 Numerical simulations of particulate suspensions via a discretized Boltzmann equation. Part 1. Theoretical foundation. *J. Fluid Mech.* **271**, 285–309.

LADD, A. J. C. & VERBERG, R. 2001 Lattice-Boltzmann simulations of particle–fluid suspensions. *J. Stat. Phys.* **104** (5), 1191–1251.

LAMSON, T. C., ROSENBERG, G., GESELOWITZ, D. B., DEUTSCH, S., STINEBRING, D. R., FRANGOS, J. A. & TARBELL, J. M. 1993 Relative blood damage in the three phases of a prosthetic heart valve flow cycle. *ASAIO J.* **39** (3), M626.

LIU, J. S., LU, P. C. & CHU, S. H. 2000 Turbulence characteristics downstream of bileaflet aortic valve prostheses. *Trans. ASME J. Biomech. Engng* **122** (2), 118–124.

MURPHY, D. W., DASI, L. P., VUKASINOVIC, J., GLEZER, A. & YOGANATHAN, A. P. 2010 Reduction of procoagulant potential of b-datum leakage jet flow in bileaflet mechanical heart valves via application of vortex generator arrays. *Trans. ASME J. Biomech. Engng* **132**, 071011.

PEES, C., GLAGAU, E., HAUSER, J. & MICHEL-BEHNKE, I. 2013 Reference values of aortic flow velocity integral in 1193 healthy infants, children, and adolescents to quickly estimate cardiac stroke volume. *Pediatr. Cardiol.* **34**, 1194–1200.

PETTERSEN, M. D., DU, W., SKEENS, M. E. & HUMES, R. A. 2008 Regression equations for calculation of $\langle i \rangle z \langle / i \rangle$ scores of cardiac structures in a large cohort of healthy infants, children, and adolescents: an echocardiographic study. *J. Am. Soc. Echocardiogr.* **21** (8), 922–934.

POPE, S. B. 2000 *Turbulent Flows*. Cambridge University Press.

SALLAM, A. M. & HWANG, N. H. 1984 Human red blood cell hemolysis in a turbulent shear flow: contribution of Reynolds shear stresses. *Biorheology* **21** (6), 783–797.

SIMON, H. A., GE, L., SOTIROPOULOS, F. & YOGANATHAN, A. P. 2010 Numerical investigation of the performance of three hinge designs of bileaflet mechanical heart valves. *Ann. Biomed. Engng* **38** (11), 3295–3310.

SLUYSMANS, T. & COLAN, S. D. 2005 Theoretical and empirical derivation of cardiovascular allometric relationships in children. *J. Appl. Physiol.* **99** (2), 445–457.

TAMBASCO, M. & STEINMAN, D. A. 2003 Path-dependent hemodynamics of the stenosed carotid bifurcation. *Ann. Biomed. Engng* **31** (9), 1054–1065.

WU, J., YUN, B. M., FALLON, A. M., HANSON, S. R., AIDUN, C. K. & YOGANATHAN, A. P. 2011 Numerical investigation of the effects of channel geometry on platelet activation and blood damage. *Ann. Biomed. Engng* **39** (2), 897–910.

YEUNG, P. K. & POPE, S. B. 1989 Lagrangian statistics from direct numerical simulations of isotropic turbulence. *J. Fluid Mech.* **207** (1), 531–586.

YOGANATHAN, A. P., FOGEL, M., GAMBLE, S., MORTON, M., SCHMIDT, P., SECUNDA, J., VIDMAR, S. & NIDO, P. 2013 A new paradigm for obtaining marketing approval for pediatric-sized prosthetic heart valves. *J. Thorac. Cardiovasc. Surg.* **146** (4), 879–886.

YOGANATHAN, A., LEO, H., TRAVIS, B. & TEOH, S. 2003 Heart valve bioengineering. In *Encyclopedia of Comprehensive Structural Integrity (CSI)*, pp. 795–796. Elsevier Science.

YUN, B. M. 2014 Simulations of pulsatile flow through bileaflet mechanical heart valves using a suspension flow model: To assess blood damage. PhD thesis, Georgia Institute of Technology.

YUN, B. M., DASI, L. P., AIDUN, C. K. & YOGANATHAN, A. P. 2014*a* Computational modelling of flow through prosthetic heart valves using the entropic lattice-Boltzmann method. *J. Fluid Mech.* **743**, 170–201.

YUN, B. M., MCELHINNEY, D. B., ARJUNON, S., MIRABELLA, L., AIDUN, C. K. & YOGANATHAN, A. P. 2014*b* Computational simulations of flow dynamics and blood damage through a bileaflet mechanical heart valve scaled to pediatric size and flow. *J. Biomech.* (in press) 10.1016/j.jbiomech.2014.06.018.

YUN, B. M., WU, J., SIMON, H. A., ARJUNON, S., SOTIROPOULOS, F., AIDUN, C. K. & YOGANATHAN, A. P. 2012 A numerical investigation of blood damage in the hinge area of aortic bileaflet mechanical heart valves during the leakage phase. *Ann. Biomed. Engng* **40** (7), 1468–1485.

ZILBERMAN, M. V., KHOURY, P. R. & KIMBALL, R. T. 2005 Two-dimensional echocardiographic valve measurements in healthy children: gender-specific differences. *Pediatr. Cardiol.* **26** (4), 356–360.